

Group 10 - Preliminary Design Report

Nadir Hamidi, Sam Taylor, Siddharth Singh

Clara Bollen Gandolfo, Krishna Chivukula, Tom Shepherd

0220368, 02201702, 02300777, 02208356, 02201684, 02023886

Abstract

This report discusses the structural design of a 500 passenger long-haul airliner designed to fly at a Mach number of 0.83 and a main cruise altitude of 30,000ft. The report goes into the loads analysis for main components on the aircraft such as the fuselage, wings, horizontal tailplane and vertical tailplane. Metallic construction is used for the wings and horizontal tailplane while composites are utilised for the vertical tailplane design. All designs both metallic and composite are optimised by finding a tradeoff between minimum weight and meeting loading requirements. For the wing and horizontal tailpane this was ensured by varying stringer geometries, skin thickness and rib spacing. For composite designs such as the vertical tailplane the layup distribution was iterated over and modified until the applied shear or compressive stress was just below 1 to ensure that the design does not contain extra mass.



28th January 2025

Contents

List of Figures	iii
List of Symbols	iv
List of tables	iv
1 Introduction	1
2 Material selection	1
2.1 Summary	1
2.2 Fuselage	1
2.3 Wings	2
2.4 Vertical tail	2
2.5 Horizontal tail	3
2.5.1 Additional Considerations	3
3 Fuselage	3
3.1 Shear Force and Bending Moment	3
3.2 Skin and Stringer Design	4
3.3 Pressure Loads	6
3.4 Light Frame Design	7
3.5 Heavy Frame Design	7
3.6 Fuselage Mass Summary	9
4 Lifting Surface	9
4.1 Load Estimation	10
4.2 Wing Box Idealisation	11
4.3 Initial Skin & Stringer Considerations:	11
4.4 Optimisation Process	12
4.5 Skin & Stringer Design	13
4.6 Spar Design	14
4.7 Ribs	15
4.8 Leading Edge Design	16
5 Empenage	17
5.1 Horizontal Tailplane	17
5.1.1 Loading	17
5.1.2 Skin and Stringers	17
5.1.3 Ribs	19
5.1.4 Spars	19
5.1.5 D-Cell Design	20
5.2 Vertical Tailplane	21
5.2.1 Loads	21
5.2.2 Composite Skin Covers	22
5.2.3 Composite Spars	23
5.2.4 Composite Ribs	24
5.2.5 D-Cell	24
5.3 Mass Calculation	25
6 Fatigue analysis	25

7 Secondary Components	26
7.1 Joints and Fittings	26
7.2 Cutouts	26
7.3 Engine mounts	27
8 Detailed Design	27
8.1 Objectives and Setup	27
8.2 Design Process	28
8.3 Pin-Joint Framework Analysis	30
8.4 Grid independence	30
9 Discussion	31
A Appendix A - Wing	ii
A Appendix C - Emmpenage	ii
A Appendix C - Detailed design	ii
A Appendix D - Code	iii

List of Figures

1	Ashby chart for σ_c index	2
2	Ashby chart for Fatigue index	2
3	Inertial Load Distribution Plotted Along the Fuselage Length	4
4	Enter Caption	5
5	Enter Caption	5
6	Structurally Compliant Stringer Parameters and Optimal Mass Point	6
7	Shear Flow around Fuselage Circumference	6
8	Direct Stress per Stringer	6
9	Stress Values in Pascals	7
10	WISE Front Wing	8
11	Heavy Frame Front Wing Spacing	8
12	WISE Rear Tailplane	9
13	Heavy Frame Rear Tailplane Spacing	9
14	Omega Section Representation	9
15	Wing Design Diagrams	10
16	Final Load Distribution	11
17	Limiting Loads For Design Purposes	11
18	Optimisation Flowchart	13
19	Optimisation Process	13
20	Skin & Stringer Design Results	14
21	Spar Design Results	15
22	Rib Thickness Distribution	16
23	LE Sizing	16
24	Horizontal Tailplane Loading	17
25	Horizontal Tailplane Loading	17
26	Stringer Pitch Limits	18
27	Second Optimisation	18
28	Second Optimisation and Final Thickness Distributions	18
29	Compressive Stress Distribution	19
30	Rib Thickness Distribution	19
31	Spar Thickness Distributions	20
32	Mass Calculation for D-Cell-Sizing for shear flow stress	20
33	Mass Calculation for D-Cell-sizing for tresca shear stress	20
34	D-Cell Thickness Distribution	21
35	D-cell Stress Distribution	21
36	Lift Force Distribution	21
37	Shear Force Distribution	21
38	Bending Moment Distribution	22
39	Torque Distribution	22
40	Skin Layup Distribution till Mid-plane	22
41	Front Spar Ply Distribution	23
42	Rear Spar Ply Distribution	23
43	Front Spar Layup till Midplane	24
44	Rear Spar Layup till Midplane	24
45	Mass variation with Psuedo-rib Number	25
46	D-Cell Thickness Distribution	25
47	Al 2024 T3 S-N Curves for Fuselage and Wing	26
48	Structural super capacitor C section beams [Emile]	27
49	Plot of Stress Distribution in raw Blank	28
50	Modified Blank	28
51	Iteration 1 of Detailed Component Obtained from Topology Optimisation	29
52	Iteration 2 - Yields at Spar Joints	29
53	Iteration 4- Does Not Yield	29

54	Final Design of Component	30
55	Pin-Joint Idealisation of Final Design	30
56	Wingbox and D-Cell Idealisation for Horizontal Tailplane	ii
57	Iteration 1 results	ii
58	Iteration 2 results	ii
59	Iteration 3 results	ii
60	Iteration 4 results	ii
61	Iteration 5 results	ii
62	Final Iteration results	ii

List of Tables

1	Final materials selected	1
2	Fuselage Component Weights and CG/ Length-wise Distribution to the Nearest Meter	4
3	Caption	5
4	Skin and Stringer Final Parameters	6
5	Light Frame Optimised Dimensions	7
6	Heavy Frame Dimensions	9
7	Fuselage Structural Mass Breakdown	9
8	Mass Calculation for Wing (1 Side)	13
9	Compressive Stress and Combined Loading Ratios for Skin Layup	23
10	Shear Stress Ratios for Rear Spar Layup	23
11	Rib Composite Layups	25
12	Mass Calculation for Vertical Tailplane	25
13	Caption: Properties of 6061-T6 Aluminium Alloy [12]	28
14	Performance of Iteration 1	29
15	Performance of Iteration 4	29
16	Performance of Final Design	30
17	Grid convergence study	31

List of Symbols

\bar{c}	Mean Aerodynamic Chord
V_S	Stall Speed (m/s)
$C_{L_{max}}$	Maximum Lift Coefficient
$C_{L_{min}}$	Minimum Lift Coefficient
$C_{L_{max,flap}}$	Maximum Lift Coefficient with Flap
$MTOW$	Maximum Takeoff Weight (kg)
$MZFW$	Maximum Zero-Fuel Weight (kg)
MLW	Maximum Landing Weight (kg)
V_C	Cruise Speed (m/s)
$C_{L\alpha}$	Lift Curve Slope (rad^{-1})
S_{ref}	Reference Wing Area (m^2)
b_{ref}	Wing Span (m)
C_{HT}	Horizontal Tail Lift Coefficient
$C_{M,0}$	Stall Moment Coefficient
c_{root}	Wing Root Chord (m)
c_{tip}	Wing Tip Chord (m)
λ	Wing Taper Ratio
$y_{eng,1}$	Distance to Engine 1 (m)
$y_{eng,2}$	Distance to Engine 2 (m)
m_{wing}	Wing Mass (kg)
$m_{nacelle}$	Nacelle Mass (kg)
m_{engine}	Engine Mass (kg)
$m_{L.G}$	Landing Gear Mass (kg)
x_{HT}	Horizontal Tail Position (m)
x_{VT}	Vertical Tail Position (m)
x_{fuel}	Fuel Position (m)
m_{fuel}	Total Fuel Mass (kg)
s_{stroke}	Stroke Length (m)
V_{vert}	Vertical Speed (m/s)
$y_{fuel-tank-start}$	Start of Fuel Tank (m)
$y_{fuel-tank-end}$	End of Fuel Tank (m)
$m_{fuselage}$	Fuselage Mass (kg)
m_{HT}	Horizontal Tail Mass (kg)
m_{VT}	Vertical Tail Mass (kg)
$S_{ref,HT}$	Reference Area of Horizontal Tail (m^2)
N_f	Fatigue Life (cycles)
σ_f	Fatigue Strength from S-N Curve (MPa)
σ_{applied}	Applied Stress (MPa)
m	Basquin's Exponent
σ_{hoop}	Hoop Stress due to Pressurization (MPa)
$\sigma_{\text{longitudinal}}$	Longitudinal Stress due to Pressurization (MPa)
P	Cabin Pressure Differential (Pa)
D	Fuselage Diameter (m)
t_{skin}	Fuselage Skin Thickness (m)
n	Load Factor
C_m	Pitching Moment Coefficient
ρ	Air Density (kg/m^3)
V	Flight Velocity (m/s)
S_{refWing}	Wing Reference Area (m^2)
MAC	Mean Aerodynamic Chord (m)
L_{HT}	Horizontal Tailplane Lift (N)
x_{cg}	Center of Gravity Position (m)
x_{acW}	Aerodynamic Center of the Wing (m)

x_{acH}	Aerodynamic Center of the Horizontal Tailplane (m)
τ_{cr}	Critical Shear Stress for Buckling (MPa)
K_s	Shear Buckling Coefficient
E	Young's Modulus (GPa)
ν	Poisson's Ratio
I_{str}	Moment of Inertia of Stringer Section (m^4)
A_{str}	Cross-Sectional Area of Stringer (m^2)
σ_{Euler}	Euler Buckling Stress (MPa)
$(EI)_{fr}$	Flexural Rigidity of Frame ($N \cdot m^2$)
C_{fr}	Frame Constant
M_d	Design Bending Moment (Nm)
b_{fr}	Frame Width (m)
q	Shear Flow (N/m)
T	Torque Applied to the Fuselage (Nm)
ϕ	Angle of Force Application (rad)
α	Dihedral Angle (rad)

1 Introduction

2 Material selection

2.1 Summary

Our material selections for each component are found below. This is an optimised selection using the appropriate merit index for each component. A mixture of aluminium alloys and composites were chosen for different structural elements.

Table 1: Final materials selected

Component	Material	Youngs modulus MPa
Fuselage skin	Aluminium 2024-T3	74
Fuselage stringer	Aluminium 2024-T861	74
Heavy frame	Aluminium 5182-H19	72
Light frame	Aluminium 2024-T861	74
Wing Upper skin	Aluminium 2024-T3	74
Wing Lower skin	Aluminium 2024-T3	74
Wing Spar	Aluminium 5182-H19	72
Vertical Tailplane skin	CFRP	Layup dependent
Vertical Tailplane spars and ribs	CFRP	Layup dependent
Horizontal Tailplane skin	Al 2024 T3	74
Horizontal Tailplane spars and ribs	Aluminium 2024-T861	74

2.2 Fuselage

The loads experienced by the fuselage include: cyclic pressurisation, internal loads, aerodynamic forces and bending moments from OEI scenarios. As such the material choice must reflect these loading cases maximising tensile and compressive strength from cyclic pressure loading cycles.

The fuselage is subjected to cyclic pressurization, internal loads, aerodynamic forces, and bending moments from OEI scenarios. Material selection must prioritize high tensile and compressive strength to withstand these conditions while ensuring structural durability.

Despite the increasing adoption of CFRP in modern aircraft, aluminium alloys remain a viable choice due to their well-characterized failure mechanisms, established manufacturing infrastructure, and superior impact damage tolerance [Reference]. Unlike composites, aluminium allows for rapid non-destructive inspection (NDI) and proven repair methodologies, reducing operational downtime [Reference]. While aluminium is heavier, advancements in Al-Li alloys enhance the specific strength and fatigue resistance, improving overall structural efficiency. Furthering this, aircraft like the Boeing 777 and Airbus A320 continue to use aluminium-heavy designs, demonstrating its viability in modern aviation. From our brief, a low cost design is specified and an Al based fuselage will meet this by reducing manufacturing costs which is passed down to the airlines and passengers.

The following merit indices were applied to determine the optimal aluminium alloy for the fuselage skin, evaluating mechanical performance, fatigue resistance, cost and density.

$$\frac{\sigma_c^{2/3}}{\rho c}, \frac{\sigma_f}{\rho c} \quad (1)$$

From the Compressive strength Ashby charts AL 2024-T861, AL 5182-H19, 2024-T3 were shortlisted. All 3 materials have excellent corrosion resistance with water and acids along with excellent UV resistance[Ashby chart ref]. To narrow the material choice down, ductility is considered to ensure the skin can easily bend around the stringers to form the required shapes. 2024-T3 is more ductile than T861 and 5 series Aluminium. Al 2024-T3 and 2024-T861 have very similar fatigue strength after 10^7 stress cycles with T3 having a higher maximum value and 5182 having a much larger fatigue strength. As such the material chosen for the skin is Al 2024-T3 with balancing all 3 factors.

The fuselage stringers require similar compressive strength requirements. However, following an industry standard conservative design approach, the skin sections are allowed to buckle at the design limit load but the stringers cannot buckle under any circumstances. The same merit indices as above were used to determine the stringer material but since ductility is not a concern for the stringers as much as the skin Al 2024-T861 was chosen due to its higher compressive strength.

The Light frames of the fuselage are light cross-section rings at closely spaced intervals. They maintain the fuselage's cross-sectional form and divide the shear-carrying skin into smaller panels which increases the critical Buckling load[Ref structures 3]. As such they will also use Al 2024 T861 due its similar loading properties as the stringers. The Heavy frames in contrast are rings at all points of high concentrated load input. As such, they require a balanced compressive and tensile strength. Fatigue is another major consideration due to repeated cycles of loading from point loads such as wing bending moments and aerodynamic forces. For Heavy frames, AL 5182-H19 is determined to be the most appropriate alloy due to its higher compressive and tensile strength properties than the other shortlisted 2 series Al alloys along with its significantly higher fatigue strength ($\approx 60\%$ higher).

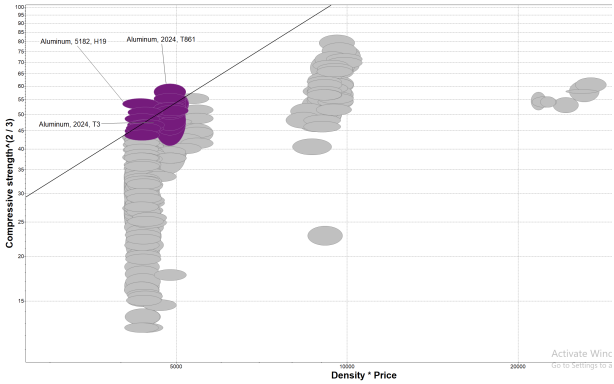


Figure 1: Ashby chart for σ_c index

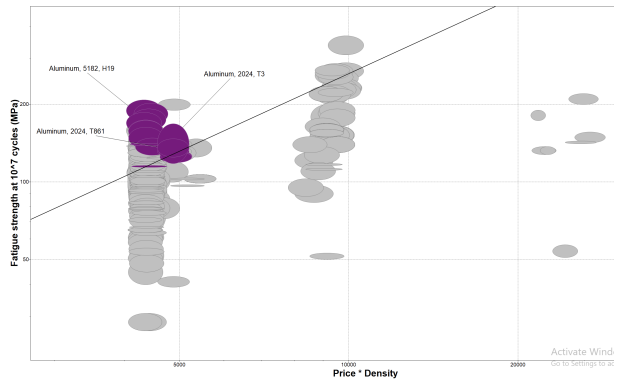


Figure 2: Ashby chart for Fatigue index

2.3 Wings

The wing can be approximated as a cantilever beam, with its root fixed to the fuselage. Consequently, it primarily experiences bending and torsion during flight. Under aerodynamic loading, the upper wing surface is subjected to compression, while the lower surface experiences tension. The material selection for the wing panels must account for minimizing deflection while also considering weight and cost constraints.

Therefore the merit index for the wing panels are chosen to be: $M_{upper} = \frac{\sigma_c^{2/3}}{\rho^{*c}}$ and $M_{lower} = \frac{\sigma_t^{2/3}}{\rho^{*c}}$. The wing spars take significant torsional loading, material selection must also consider the torsional stiffness-to-weight ratio. The appropriate merit index for selecting the spar material, assuming a thin-walled circular or box section, is thus: $M_{spar} = \frac{G^{1/2}}{\rho c}$. From Ashby charts, Al 2024 T3 was chosen for the top and lower skins with Al 5182 H19.

2.4 Vertical tail

The vertical tail experiences significant bending and torsional loads, especially at its root, where it interfaces with the fuselage. It must withstand aerodynamic loads, yawing manoeuvres, and inertial forces while maintaining integrity. Due to their smaller size relative to the rest of the aircraft the cost of using CF will not be as high compared to using a composite on larger components such as the fuselage. Therefore, the vertical tailplane skin spars and ribs will be made from CFRP instead of GLARE such as what was used on the A380 due to its more prevalent use on modern aircraft.

A CFRP laminate with a quasi-isotropic layup is chosen for the vertical tail, ensuring balanced mechanical properties in multiple loading directions. The layup consists of 0° , $\pm 45^\circ$, and 90° plies, with an emphasis on $\pm 45^\circ$ orientations to enhance shear resistance and torsional stiffness. This laminate stacking sequence aims to reproduce more isotropic behaviour in-plane by distributing fibre orientations in multiple directions. This results in nearly uniform mechanical properties across different in-plane load directions. To maintain the integrity of the laminate, no more than 70% of plies are in the direction of the load,

and no less than 10% of plies are in each of the other directions. A high-modulus carbon fibre will be used to maximize stiffness and minimize deflections along with toughened epoxy resin to improve damage tolerance and resistance to impact. Auto-clave cured Pre preg twill is the weave of choice for ease of manufacture with the curved surface of the Vertical tail.

2.5 Horizontal tail

The Vertical tailplane is a more isolated structure, making composite construction more feasible without significantly affecting other aircraft components whereas the Horizontal tail plane is subject to a higher risk of ground damage from runway debris due to its lower position. This makes metal more preferable as a skin material here due to its higher impact tolerance[Ref]. Also, the vertical tail is generally smaller than the horizontal tail. So, it's cheaper to use expensive composites for the vertical tail as opposed to the horizontal.

The spars for the horizontal tailplane will be made out of CFRP and the vertical well be AL 2024 T861

2.5.1 Additional Considerations

Leading Edge Protection: The leading edges of both the VT and HT are prone to impact damage from bird strikes and debris. To enhance toughness, a thin titanium leading edge is integrated, reducing chance of premature failure from impacts such as birdstrikes. To prevent delamination an industry standard minimum laminate thickness of 1.5 mm[ref] will be used with the ply thickness set at 0.125 mm.

3 Fuselage

Fundamental to the structural analysis of the aircraft is considering the loading limitations of the fuselage. Failure to carefully assess this area could lead to structural damage, risking the safety and integrity of the aircraft. This section will analyse three loading cases on the aircraft as listed below.

1. The first load case explored was symmetric flight at the ultimate load factor 3.75. For the context of the shear force and bending analysis, the dive speed V_d was applied as it constitutes a more limiting case.
2. The second case explored was a One Engine Inoperative (OEI) case. The more limiting case occurs when an outer engine is inoperative as the resultant yawing moment is higher. We modelled a restorative force acting through the aerodynamic center of the vertical tailplane to counteract this yawing moment. A resultant rolling moment is considered later on in the calculation of shear force. The OEI case was considered at a loading factor of 1 at the dive speed as per CS 25.362. [?]
3. The third case is landing with the nose gear off where the main undercarriage supports the load of the full plane.

Furthermore this section will lay out the optimisation process for the fuselage skin, stringer, light frame and heavy frame design. The dimensions for each were optimised, constrained by material yield and buckling considerations. Each was optimised using a parametric sweep approach, analysing all possible combinations for structural compliance, and picking the combination that minimised the relevant objective value or function.

3.1 Shear Force and Bending Moment

To understand how internal forces are distributed along the fuselage under loading, we analysed the shear force and bending moment. The first step was to discretise the inertial loads of the aircraft. Fuselage, furnishings, payload and fuel were distributed along their respective areas. The remaining major components were modelled as point loads along the fuselage. This distribution is plotted in Figure 3. A breakdown of the loads is given in table 2.

In terms of air loads we consider the load that the tailplane would need to produce to keep the aircraft trimmed. This was then used to calculate the internal reaction forces at the wing spars with Equations (2) and (3).

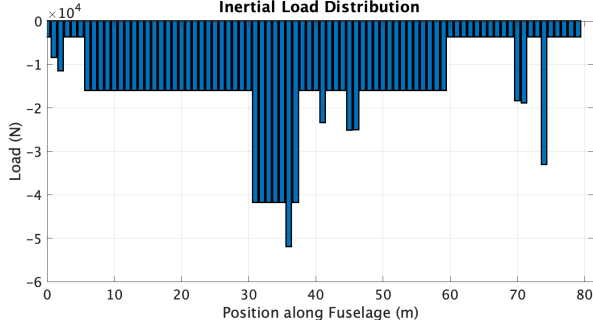


Figure 3: Inertial Load Distribution Plotted Along the Fuselage Length

Component	Weight (kg)	x_{cg} (m)
Fuselage	29,744	0 - 79
Horizontal Tailplane	2,998	75
Vertical Tailplane	1,552.8	72
Nose Landing Gear	486.52	2
Fuel Systems	936	46
Flight Controls	927	47
Installed APU	1,496	71
Instruments	796.77	3
Electronic System	1,037	37
Furnishing	17,227	6 - 61
Anti Icing System	757.9	42
Payload	51,879	6 - 61
Fuel	156,760	31 - 39

Table 2: Fuselage Component Weights and CG/ Lengthwise Distribution to the Nearest Meter

Next, we considered the trimming airload produced by the horizontal tailplane and the respective reaction forces at the wing spars. The tailplane force was calculated using [14]:

$$MoW = n \cdot C_m \cdot (0.5 \cdot \rho \cdot V^2 \cdot S_{refWing} \cdot MAC) \quad (2)$$

$$LHT = \frac{-MTOW \cdot 9.81 \cdot (x_{cg} - x_{acW}) + MoW}{x_{acH.1} - x_{acW}} \quad (3)$$

To model our load cases of interest, our maximum load factor $n = 3.75$, landing load factor $n=2.18$, OEI load factor $n = 1$ and minimum load factor $n = -1.5$ were used. For each, the reaction forces at the wing spars were calculated by solving equation (4).

$$\begin{bmatrix} x_{front\ spar} & x_{rear\ spar} \\ 1 & 1 \end{bmatrix} \begin{bmatrix} Force\ RF \\ Force\ RR \end{bmatrix} = \begin{bmatrix} Total\ Moment \\ Total\ Load \end{bmatrix} \quad (4)$$

In a One Engine Inoperative scenario, the thrust differential has a yawing effect on the overall aircraft. To counter this, a rudder input is used, introducing an extra lateral load. As a result of this force, a rolling moment is induced as the force acts at a vertical offset to the engine line of action. This moment was calculated to be $1.7502e+06$ Nm. The restorative aileron input required was modelled as acting at the halfway along the semi-span at the rear spar at a magnitude of $1.0771e+05$ N.

The reaction loads and tailplane air load (and aileron input load in the OEI case) were then superposed with the inertial fuselage loads and summed cumulatively to create a shear force distribution along the fuselage. Figure 4 is a plot of the shear force of the four load cases previously discussed, against fuselage x-position. The most constraining load case was subsequently identified as the $n=3.75$ symmetrical flight case, across the length of the fuselage.

From this point the MATLAB `cumtrapz()` function was used to gather the bending moment distribution for each case, shown in Figure 5.

At this point the max shear force was divided by the material shear modulus resulting in a critical skin thickness value of 4.2mm. Unless stated otherwise explicitly, the rest of the fuselage preliminary design uses the maximum load factor of 3.75 so that the most constraining case is analysed.

3.2 Skin and Stringer Design

The material chosen for the fuselage skin was Aluminium 2024-T3 and the material for the fuselage stringers was Aluminium 2024-T861. The relevant properties for the skin and stringer design are tensile yield stress, shear yield stress, Young's modulus and density. They are tabulated in Table3.

A Z-section shape was chosen due to it's wide industry popularity and weight-saving advantages [15]. Before optimising, it was important to understand the structural constraints of the aircraft. Both the skin

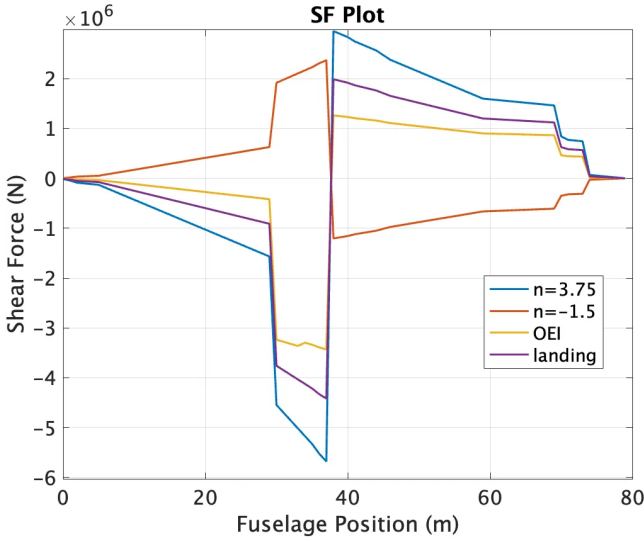


Figure 4: Enter Caption

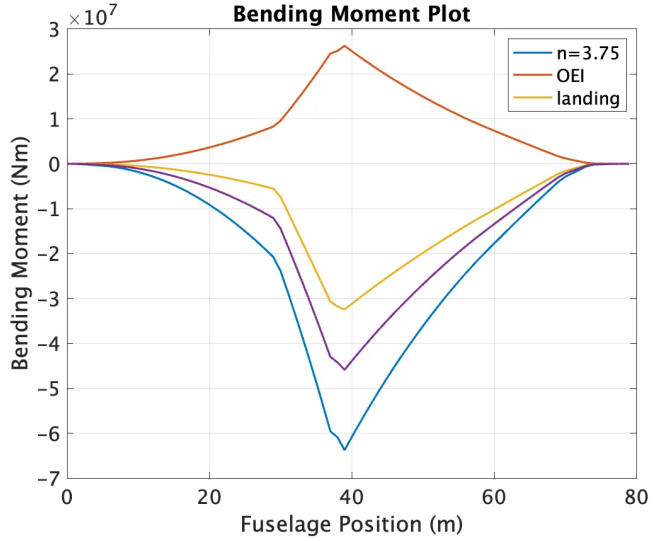


Figure 5: Enter Caption

	Material	Tensile σ (MPa)	Shear σ (MPa)	E (GPa)
Skin	Aluminium 2024-T3	331	290	73
Stringer	Aluminium 2024-T861	490	310	71

Table 3: Caption

and stringers would be liable to failure through material yield and buckling.

1. Stringer Yield: To check if the stringer will yield we calculate the direct stress felt by each stringer and then compare the maximum value in that set to the yield stress of the material. [16]
2. Stringer Buckling: To check the stringer buckling we calculate the cross-sectional stringer area and moment of inertia I_{xx} . This is plugged into equation (5).

$$\sigma_{\text{euler}} = \frac{\pi^2 EI_{\text{str}}}{A_{\text{str}} L^2} \quad (5)$$

3. Skin Yield: Dividing the total maximum shear flow by the skin thickness gives the maximum shear stress the skin will bear. This is compared against the shear yield stress of the material.
4. Skin Buckling: Finally the skin and stringer parameters must result in a shear stress lower than the critical buckling stress as defined in equation (6).

$$\tau_{\text{cr}} = K_s \cdot \frac{\pi^2 E}{12(1 - \nu^2)} \cdot \left(\frac{t_{\text{skin}}}{s_{\text{stringer}}} \right)^2 \quad (6)$$

The optimisation approach used was a parametric sweep across the following variables: skin thickness, stringer spacing, stringer thickness, web height and flange length. The purpose of the optimisation is to reduce the mass of the stringers along the fuselage, therefore the result of interest for each combination was the number of stringers multiplied by the cross-sectional area per stringer. If the combination of variables of a given iteration satisfied the four structural requirements listed above, that combination was added to the viable design space. Finally, of the viable combinations, the group that minimised cross-sectional area by number of stringers (our objective function), was selected as set of dimensions of the final skin and stringer design. Sensible upper and lower testing bounds were selected for each parameter based on industry current industry norms. Our skin thickness however had a necessary lower bound of 4.2mm corresponding to the maximum shear stress divided by the shear yield stress of the material as discussed in the previous section. The final skin thickness was increased through the optimisation to 4.5mm which though seemingly counter-intuitive for mass minimisation, a greater skin thickness allowed for greater stringer spacing without skin buckling, thus reducing our total stringer number. Figure 6 is a plot of the design space with stringer thickness, spacing and height plotted. This is illustrative of the outcome of

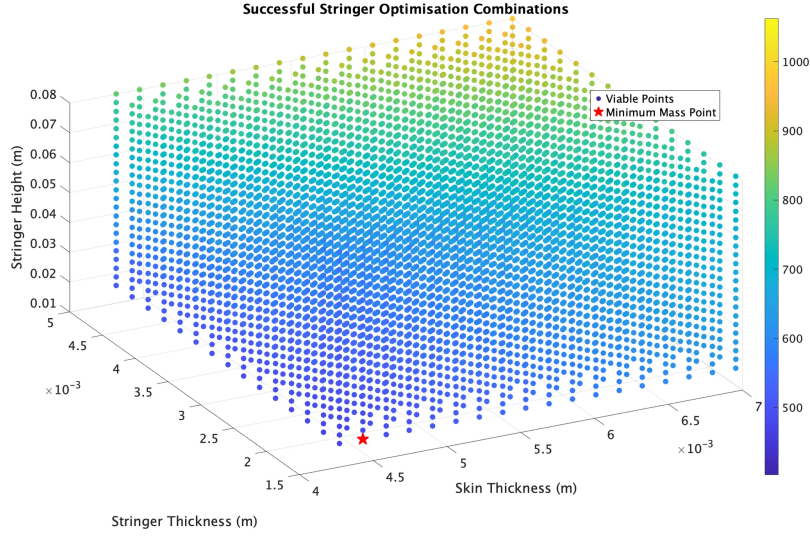


Figure 6: Structurally Compliant Stringer Parameters and Optimal Mass Point

the optimisation, though there are five parameters being varied. The starred point marks the lowest total stringer mass option of the parameter sweep. The dimensions corresponding to this point are in Table 4.

Pitch (m)	t_{stringer} (m)	H_{web} (m)	L_{Flange} (m)	Area (m^2)	Num. Stringers	t_{skin} (mm)
0.1529	0.0045	0.0158	0.01	3.6160e-05	131	4.5

Table 4: Skin and Stringer Final Parameters

Having calculated our optimised skin and stringer dimensions/parameters we can then plot our shear flow and direct stress plots around the fuselage circumference as seen in Figures 7 and 8.

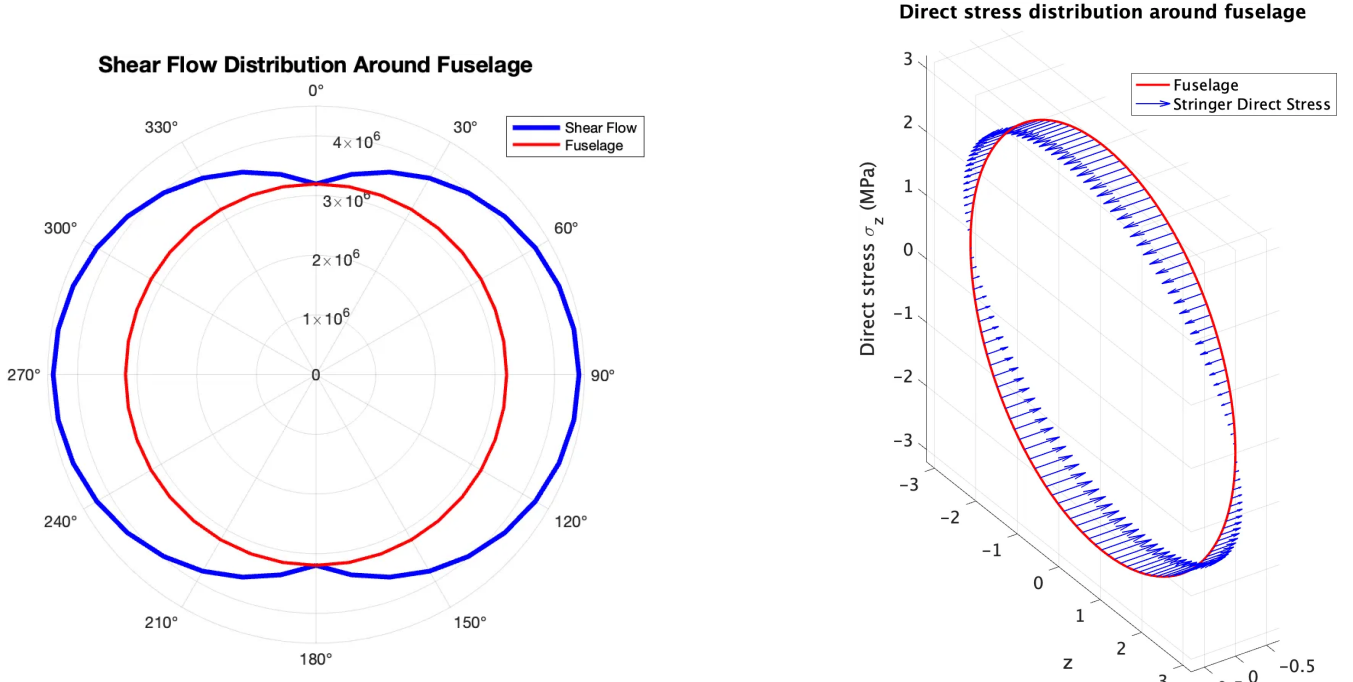


Figure 7: Shear Flow around Fuselage Circumference

Figure 8: Direct Stress per Stringer

3.3 Pressure Loads

To analyse the effect of pressurisation on the fuselage, the hoop and longitudinal stressed were calculated. Our aircraft cabin is pressurised at 5,500ft. Cabin pressure is subtracted from atmospheric pressure to give a pressure load of 0.5079 bar.

For the hoop stresses: $\left(\frac{\sigma_H}{P}\right) = \left(\frac{D}{2t_{\text{skin}}}\right)$ (7)

Stress Type	Value (MPa)
Hoop Stress (σ_h)	17.5
Longitudinal Stress (σ_l)	8.75

For the longitudinal stresses: $\left(\frac{\sigma_L}{P}\right) = \left(\frac{D}{4t_{\text{skin}}}\right)$ (8)

Figure 9: Stress Values in Pascals

To work out the minimum required skin thickness to withstand the pressure loads acting on the fuselage we used equation (9). This gave a minimum skin thickness of 0.3404 mm. Given that the shear stress condition is more constraining and requires a higher skin thickness, the result from pressure load analysis was disregarded.

For the required skin thickness due to pressure: $t_{\text{skin,pressure}} = \frac{D \cdot P_{\text{atm}} \cdot P}{2\sigma_{\text{yield}}}$ (9)

3.4 Light Frame Design

Having sized our stringers and looked at the pressure loads, the next step is to design and optimise the light frames that run along the length of the fuselage, both keeping the shape of the fuselage in tact whilst bearing the associated structural loads.

The frame section of choice was a C-section due to its appropriate structural performance and mass balance and wider industry adoption compared to other frame shape options. [16]

As with the stringer procedure, we optimised the light frame dimensions and spacing using a parametric sweep within sensible industry-norm values. Equation (10) is used to evaluate the critical moment of inertia for a given frame spacing. Equation (11) is then used to calculate the I_{xx} of the current combination of parameters. These values are then compared and if the combination I_{xx} is greater than the critical value, the combination of parameters is saved to the successful design space.

$$(EI)_{fr} = \frac{C_{fr}Md^2}{b_{fr}}$$
 (10)

$$I_{xx,fr} = \frac{t_{fr}h_{fr}^3}{12} + \frac{w_{fr}t_{fr}h_{fr}^2}{2}$$
 (11)

The objective function in this case was the area of each frame cross section multiplied by the number of frames, affected of course by the frame spacing. Our variables were the web height, the length of the two flanges, the sectional thickness and the frame spacing. Iterations were initiated from a spacing of 0.5m as this is the recommended allowance to fit around the cabin windows. [16]

The resultant dimensions of the C frame from the optimisation can be seen in Table 5.

Web Height (m)	Flange Length (m)	Thickness (m)	Spacing (m)	Number of Light Frames
0.1119	0.0856	0.0075	0.5645	132

Table 5: Light Frame Optimised Dimensions

3.5 Heavy Frame Design

At key points in the fuselage, larger, heavy frames were placed to add an appropriate load path for the comparatively large loads. The heavy frames sized were located as follows: at the front spar of the wing, at the rear spar of the wing, at the front spar of the tailplane and at the rear spar of the tailplane. Our horizontal and vertical tailplane are mounted with leading edges aligned, at given that the horizontal tailplane is only 0.2m longer than the vertical tailplane, the spars were assumed to be aligned with respect to x-position along the fuselage. Furthermore a nose landing-gear frame was not sized as it is not considered in the three load cases detailed at the start of this section.

The first step was to generate WISE curves and analyse maximum normal forces, shear forces and bending moments. At each heavy frame location the most constraining load case of $n = 3.75$ was considered.

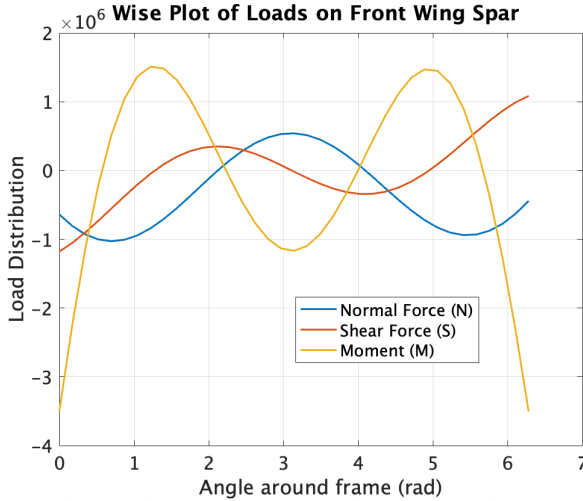


Figure 10: WISE Front Wing

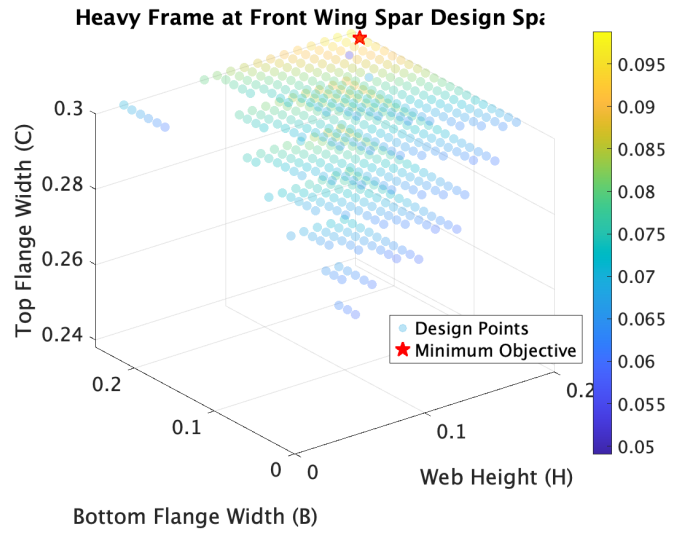


Figure 11: Heavy Frame Front Wing Spacing

The wing of the aircraft is mounted at a dihedral angle of 5 degrees. As a result, the point loads acting at the spars from these points are not purely radial; they have a tangential component. The shear forces at the wing spar locations were decomposed into the two components and the normal stress, shear stress and bending stress along the circumference of the fuselage were solved derived from Equation (12).

$$q = \left[\frac{T + Pr}{2\pi r^2} + \frac{P \cos(\phi - \alpha)}{\pi r} + \frac{Q \sin(\phi - \alpha)}{\pi r} \right] \quad (12)$$

At the tailplane spars, given that the horizontal stabiliser is mounted parallel to the horizontal axis of symmetry, the point loads were considered as exact radial loads. Had load case 2 (OEI) been a more constraining case than $n=3.75$ then the analysis would have included tangential and torque loads. The radial loads at the front and rear tailplane spar locations were then used with the same equations to solve for the three respective stresses along the fuselage circumference. Having produced these stress distributions they were then plotted as WISE curves. The rear tailplane and front wing heavy frame wise plots are shown in Figures 10 and 12.

As was done for stringer and light frame optimisation, a parametric sweep optimisation approach was adopted. As the heavy frames are placed in select locations, unlike before the number of frames does not factor into the optimisation problem. The objective function is therefore strictly a measure of cross-sectional area. It became apparent early on that the initially chosen I stringer was unable to withstand the maximum loads at these key positions unless it had disproportionately large dimensions. As a result due to its high strength to weight ratio and load-bearing properties, an omega section was used as the final section shape to optimise.

In Figures 11 and 13 are 3D plots representing the design space of successful combinations within the upper and lower bounds tested for variables h , b , c and t (See Figure 14 for the variable definitions). The methodology in this particular optimisation was as follows:

1. Set upper and lower bounds of h , b , c and t .
2. Set ratios of h/c , c/b and c/t to ensure output dimensions produce reasonable omega sections.
3. Compute the cross-sectional area and I_{xx} of the combination
4. Check that the maximum direct stress, shear and bending stress (the loads being taken from WISE plots) don't exceed material yield limits.
5. If the combination successfully passes the prior structural compliance test, the solution is added to the design space. If not, the solution is discarded.
6. Of the solution space, the combination which yields the lowest cross-sectional area is chosen as the final design point.

This process was repeated for each of the four heavy frame locations. The final values are tabulated in Table 6.

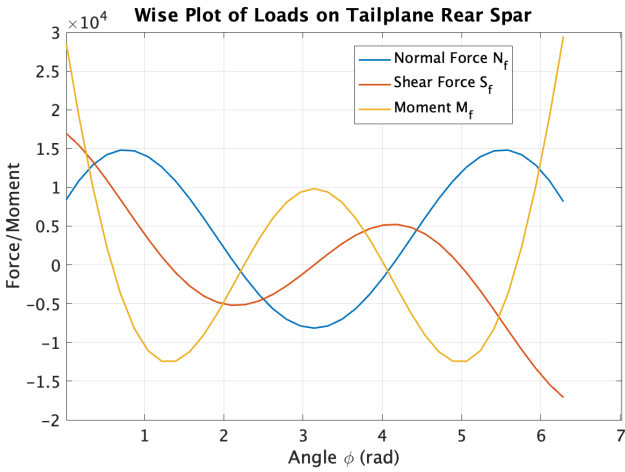


Figure 12: WISE Rear Tailplane

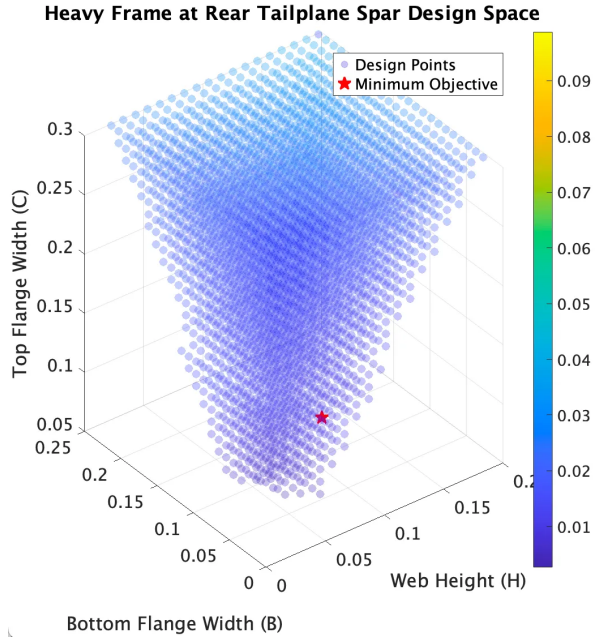


Figure 13: Heavy Frame Rear Tailplane Spacing

	h (mm)	b (mm)	c (mm)	t (mm)
Wing Front	196.9	238.1	300.0	42.0
Wing Rear	196.6	207.2	300.0	65.9
Tailplane Front	196.9	248.4	300.0	14.7
Tailplane Rear	73.3	42.2	124.7	7.8

Table 6: Heavy Frame Dimensions

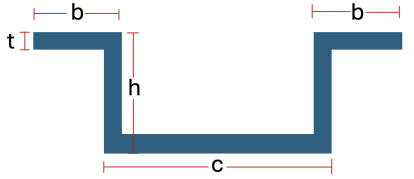


Figure 14: Omega Section Representation

3.6 Fuselage Mass Summary

To conclude the section on fuselage structural analysis, Table 7 provides a breakdown of the components previously designed. The skin mass was modelled with the nosecone as a hollow cone, the rear of the aircraft from the onset of aft sweep as a hollow frustum and the rest of the aircraft (broadly cabin area) as a hollow cylinder. The final fuselage mass came out to 25,868kg. Our conceptual design phase had estimated the fuselage mass to be 29,744kg. Though this appears to be an excellent estimate, the analysis of this report has excluded major fuselage weight adding components such as screws, windows, doors etc. The assumption then becomes that the initial estimate of mass was an underestimate. The decision to proceed with a skin thickness above the minimum requirement to reduce the stringer and frame number likely also contributes to the higher fuselage mass.

Component	Mass (kg)
Stringer Mass	1,500.7
Skin Mass	16,300.0
Light Frames	3,138.9
Heavy Frames	8,067.7
Total Fuselage Mass	25,868

Table 7: Fuselage Structural Mass Breakdown

4 Lifting Surface

This section of the report aims to describe the load estimation and structural design optimisation methods employed to analyse the different in flight shear, bending and torque loading conditions, and engineer a

suitable structure. The conditions relevant to the structural design of the wing are landing and cruise at the ultimate load factor as these were the most constraining conditions with the greatest loading. What follows is a description of the geometric parameters, which we had the freedom to change, and the mathematical foundation of how these were iterated during the overall structural and mass saving optimisation process. The structural components designed were the upper and lower skin, stringers, spars and ribs, as well as the leading edge, resulting in the wing schematic presented in Figure 15a.

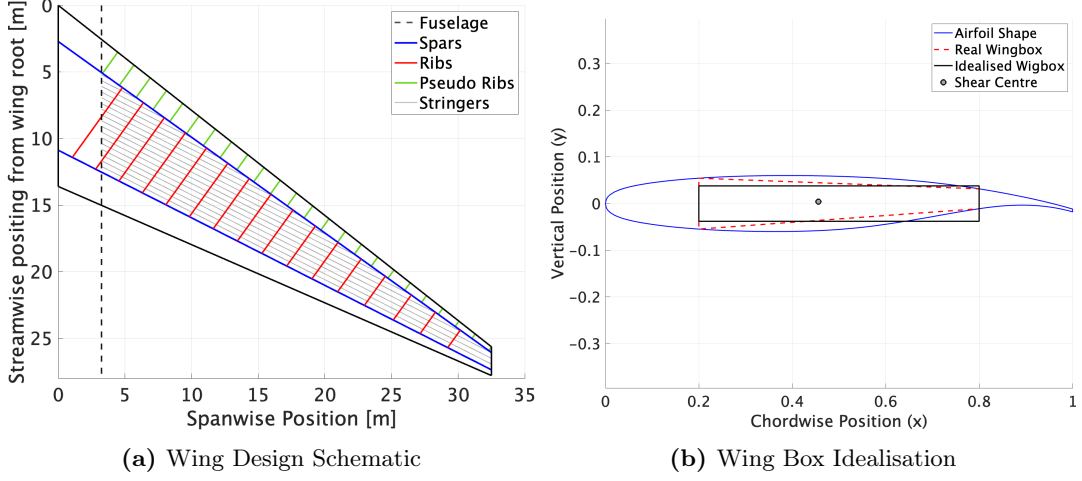


Figure 15: Wing Design Diagrams

4.1 Load Estimation

Before starting the design of these components, it was necessary to derive a model to describe the loading conditions and magnitudes encountered. The loads were broken down into inertial, aerodynamic and ground loads.

Inertial loading of the wing was determined by summing the self-weight of the wing and the fuel weights distributed along the wing, as well as point loads representing the engines and landing gear spread over a single discretisation. The wing was assumed to be made of a uniform material throughout the span, following a constant 0.25 taper ratio outlined in the Conceptual Design Report [2]. The fuel weight was distributed within the fuel tanks following this same taper. Hydraulic, fuel, and anti-icing systems were assumed to be uniformly distributed along the wing as their position were not determined during this design phase. To incorporate the load factors, the mass distribution was multiplied by ng . Following the guidance in CS 25 [1], the limiting load factors are +3.75g and -1.5g.

Aerodynamic loading was calculated by assuming an elliptic lift distribution and enforcing that the area beneath the distribution was equal to the weight of the aircraft. Two correction factors were applied to the span of the wing. The first enforces the fact that only the wetted portion of the wing produces lift. The second accounted for the sweep of the wing and its flexural axis.

For ground loading the landing load factor was calculated from the acceleration of the aircraft during landing using Equation (13). With knowledge of the landing gear deflection from Conceptual Design [2] and regulatory constraints on the vertical landing speed from CS 25 [1], the acceleration was 2.18g.

$$n_{\text{landing}} = \frac{1}{2g} \frac{dV_{\text{vert}}^2}{ds_{\text{L.G.}}} = 2.18g \quad (13)$$

A plot of the total load distribution considering each of the inertial, aerodynamic and ground loads is given below in figure 16, note that although the loading cases were also calculated at a load factor of -1.5g, they are not shown in this plot as they were less constraining for later analysis.

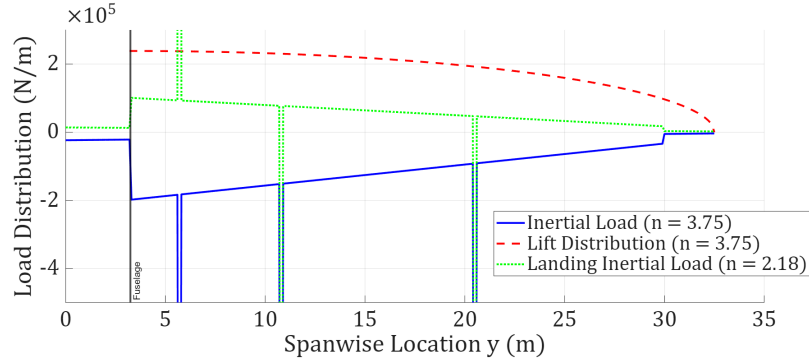


Figure 16: Final Load Distribution

To obtain the shear force and bending moment distributions, the load distribution were integrated in the spanwise direction starting from the wing tip, this was implemented by performing a cumulative trapezoidal summation. Starting the integration from the wing tip ensure that the correct boundary conditions are enforced and can be validated in figure 17.

To determine the torque load, it was necessary to locate the forces acting on the wing in the chordwise direction. The flexural axis was assumed to lie centrally between the front and rear spar at 50% of the chord. This served as a basis from which to measure the moment arms of the other forces acting on the wing. The aerodynamic loading was located at the quarter chord point, the wing structural weight was assumed to be located at the point of maximum thickness of the aerofoil section at 37% chord. The fuel weight was assumed to act through the centroid of the true trapezoidal wing box at 48% chord. The landing gear is attached to the rear spar, thus its load was located at 80% chord. Finally, the thrust was applied through the engine centre 2.3m from the flexural axis.

Plots for the final shear, torque and bending moment distributions are given in Figure 17, these represent the most limiting combinations of the different types of load experienced throughout all flight conditions. As expected, most of these loads stem from the 3.75g manoeuvre limit, but the landing load played a significant role in the shear loading, particularly near the wing root, as seen by the characteristic step increase in shear.

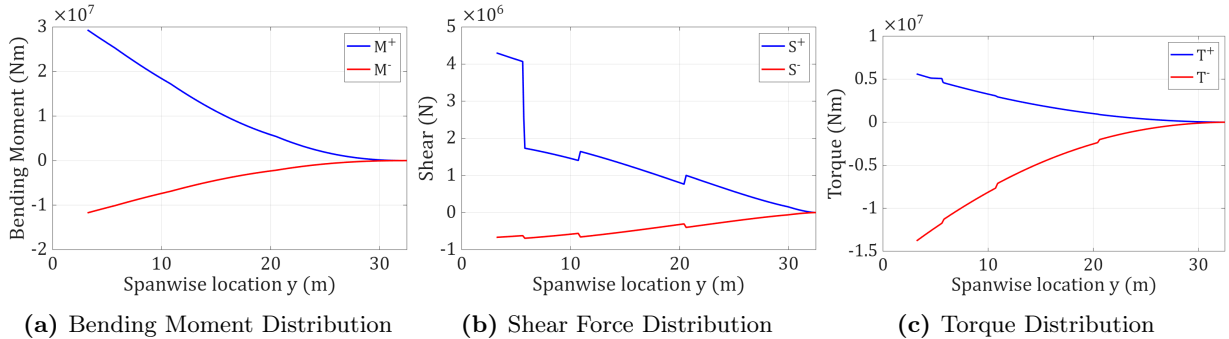


Figure 17: Limiting Loads For Design Purposes

4.2 Wing Box Idealisation

Throughout this design process, the wing box was idealised as a rectangle shown by Figure ???. The height of this rectangle was modelled as the average of the aerofoil thickness at the front and rear spars, located at $0.2c$ and $0.8c$ respectively. The simplification of a rectangular wing box eased design processes such as the spar design and was chosen as opposed to a trapezoidal wing box. Analysis was further simplified as the height of the wing box scaled linearly with the spanwise chord distribution of the wing.

4.3 Initial Skin & Stringer Considerations:

Stringers are structural members located internal to the wing box, running in the spanwise direction along the upper and lower skin. They split the otherwise continuous skin into a series of panels, improving buckling resistance and allowing for a reduced skin thickness. The stringers in conjunction with the

skin are responsible for carrying the bending moment and the shear force arising due to torque loading. Considering the bending moment plots shown in Figure 17, it is evident that the upper skin will be in compression, while the lower skin is in tension. These load plots also illustrate that the most constraining loading case considered is that of compression, and it can be concluded that a skin design which is sufficient to resist this loading case will thus be sufficient to resist the less limiting tension case.

There exists a vast number of stringer types, each with their own benefits and drawbacks. Fully enclosed area stringers, such as Y or hat stringers were immediately discounted as these introduce considerable inspection difficulties with moisture accumulation and corrosion. Although, it is worth noting that recent manufacturing advancements have seen closed Omega sections implemented in the structural design of the A350 [17]. Considering those which are most commonly utilised for aerospace structures, open sections such as J or Z sections presented a viable alternative. Due to the wealth of empirical data, heritage and overall performance, the Z section was chosen.

The Z stringer has the following design parameters. Flange width d , web height h , flange to web ratio $\frac{d}{h}$ and stringer thickness t_s . Regarding the flange to width ratio, there are only certain values for which experimental data is available, namely the following ratios, 0.3 [4], 0.4 and 0.5 [5]. In order to implement this data into the optimisation process, the plots were digitised and used to interpolate the relevant values. By selecting a single ratio this process was significantly shortened, as such, the ratio $\frac{d}{h} = 0.3$ was selected. This choice has in effect reduced the number of free variables from four to two, either d or h and t_s .

4.4 Optimisation Process

Another variable that needed to be decided was the stringer pitch, which dictates the number of effective panels the skin was split into. The formulas employed in the skin design are developed later, but the principle of their optimisation can be explained now. The process was implemented in MATLAB and starts by defining a sensible range of values for the three variables h , b_1 and t_s , these are taken as input by the structural analysis code and each combination of these variables was analysed. The code outputs whether the relevant criteria have been enforced and determines if the given combination of design variables was feasible or invalid. To account for manufacturability of these designs, the idealised continuous thickness distributions were replaced with stepped distributions with 1mm increments. The feasibility of these new designs was then be rechecked, and now invalid results removed. This process is illustrated in figure 22. To assess which designs were superior, the total effective thickness of the ribs and skin could be calculated, according to the formula given by Farrar[4]:

$$T + \frac{DT_R}{L} = t_{\Sigma \text{eff}} \quad (14)$$

Minimising this function was equivalent to finding a minimum mass design. Therefore, the optimal design was the one with the lowest effective thickness distribution along the span. In total, 1144 different design combinations were tested, of which, 107 fulfilled all the checking criteria. Upon applying the manufacturability constraints to these combinations, this number was further reduced to 23. This process is illustrated in figure 19. The values for the different design parameters were initialised as follows:

- t_s : 3mm to 10mm in 1mm steps
- b_1 : 0.25m to 0.85m in 0.05m steps
- h : 50mm to 100mm in 5mm steps

Of the combinations trialled, the most optimal solution corresponded to the following stringer parameters: $t_s = 9\text{mm}$, $b_1 = 0.5\text{m}$ and $h = 90\text{mm}$. This geometry is the one on which all following calculations are made, and is shown in figure 15a. The calculated mass of the wing structure is given in table ??

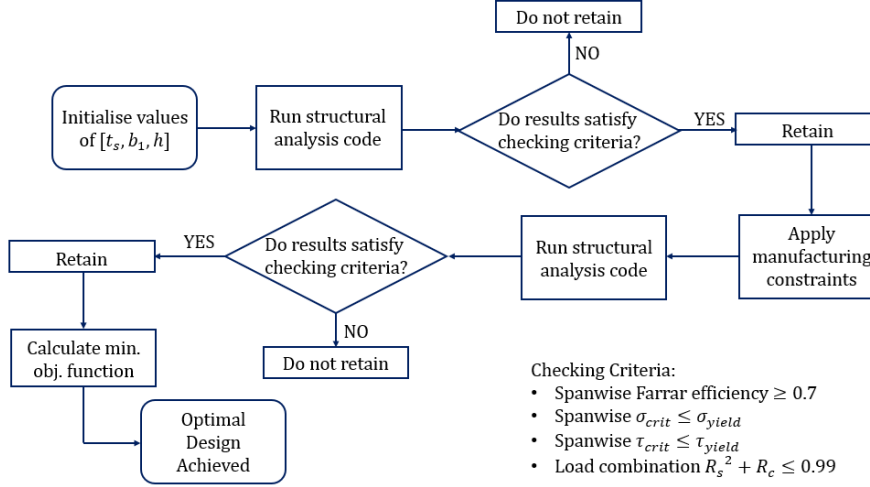


Figure 18: Optimisation Flowchart

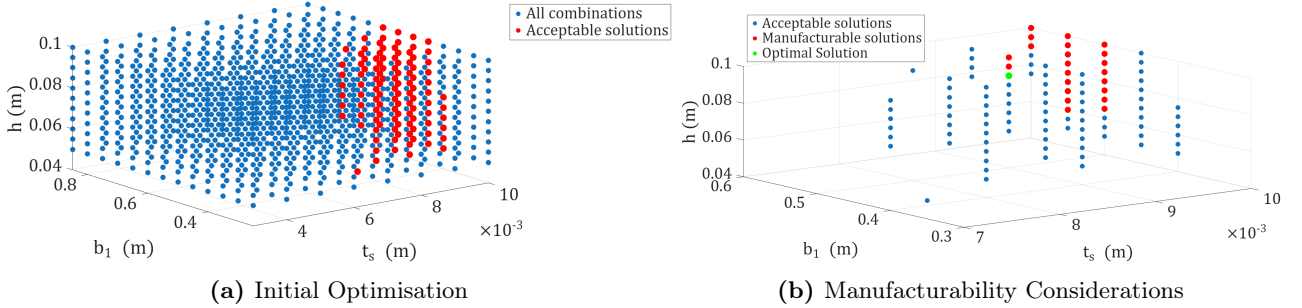


Figure 19: Optimisation Process

Table 8: Mass Calculation for Wing (1 Side)

Component	Mass (kg)
Skin and Stringers	5106.4
Ribs	677.7
Front Spar	798.5
Rear Spar	463.4
D-Cell Panel	528.4
Total Mass	7570.8

4.5 Skin & Stringer Design

The role of the skin and stringers is to take, in its entirety, the compressive load applied to the wing. Due to the compressive nature of the stresses in the wing, local and global buckling of the skin panels, as well as flexural stringer buckling must be considered. Finally, a consideration of failure by yielding must be made. For optimal material efficiency, it can be enforced that the critical global and local buckling stress of the panels coincide, leading to the following formula for the effective skin thickness:

$$\sigma = 3.62E \left(\frac{t_{eff}}{b_1} \right)^2 = \frac{M}{b_2 c t_{eff}} \rightarrow t_{eff} = \sqrt[3]{\frac{M b_1^2}{3.62 c b_2 E}} \quad (15)$$

This means that the skin thickness will always be large enough to resist the limit load bending moment, but it neglects to analyse the yielding performance. The method outlined by Catchpole [4] provides a corrective factor to calculate the critical stress for different combinations of stringer to skin, thickness and

area ratios. This value was used to check whether the stress seen in the skin is below the yield stress of the material and is used as one of the several checking criteria for the structural sizing code. Following the same logic of maximising the material efficiency, we enforce that the flexural stringer buckling is equal to the global critical buckling according to the following formula:

$$\sigma = F \sqrt{\frac{NE_T}{L}} \quad (16)$$

With prior knowledge of the stress distribution throughout the wing, the only remaining value to find is the Farrar efficiency F . Using the same plot digitisation method as employed with the Catchpole diagram, a spanwise distribution of the Farrar efficiency along the span was found, and then employed in equation 16. Another checking criteria which was employed in the code ensures that at no point along the span does the efficiency ever drop below 0.7. Efficiencies of 0.7 upwards are what are typically considered efficient designs, and by employing this constraint, the code automatically removed any non-efficient design combinations. By enforcing that the global and stringer buckling coincide, we were able to extract from equation 16, the optimal spanwise rib spacing. Knowing the rib spacing at the root, the spanwise location of the second rib was found and by repeating this process, the rib locations across the entire span were found, resulting in 16 ribs. Plots of the ideal and manufacturable skin thickness are given in figure 20, alongside the spanwise Farrar efficiency and optimal rib spacing.

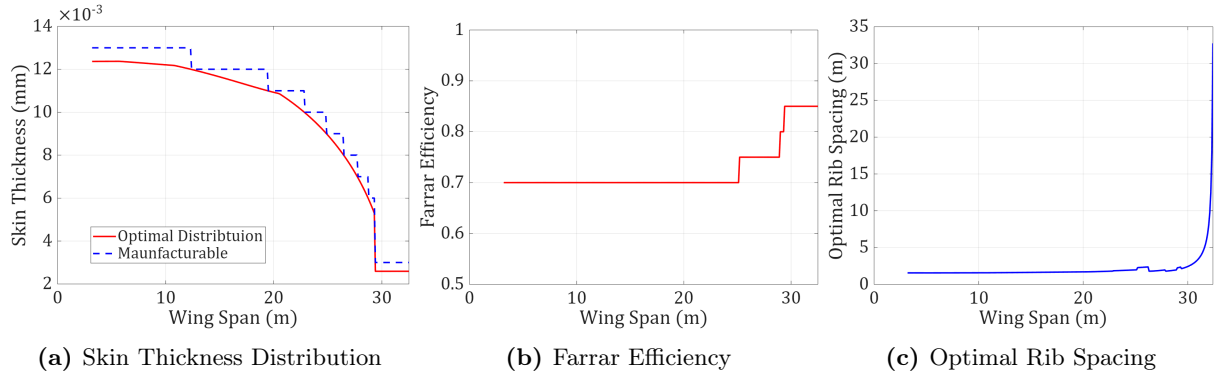


Figure 20: Skin & Stringer Design Results

4.6 Spar Design

The spars of the wings were designed to withstand the shear and torque loading encountered during operation. This loading gives rise to shear flow within the structure, with the shear flow due to the shear forces acting only in the front and rear spar, while the shear flow due to the applied torque acts throughout the wing box. This means that the shear flows in the front and rear spars can be given respectively by:

$$q_{fs} = q_{\text{shear}} + q_{\text{torque}} \quad q_{rs} = q_{\text{shear}} - q_{\text{torque}} \quad (17)$$

It was assumed that the wing box would be capable of carrying the torque loading in its entirety and the D-cell would not be a load bearing member. This is due to the heavy usage of leading edge slats and the actuation systems that must be employed to provide their functionality. By designing only the wing box to take the torque, we have also produced a more conservative design; one which is better suited in the event the D-cell is compromised by a bird strike.

By equating the shear stress and the panel buckling stress, the thickness distribution of the two spars can be found. Again, as we are considering the buckling performance of a structural element, stiffeners can be introduced along the length of the spar, effectively splitting the spar into a finite number of smaller plates. According to the following formula for the spar thickness distribution:

$$t_{\text{spar}} = \sqrt[3]{\frac{qb_2}{K_s E}} \quad (18)$$

The spar thickness can be significantly reduced by increasing the shear buckling factor. The maximum value that can be attained for this factor is 13.4 when the height of the spar and the stiffener spacing

coincide [6]. To assess whether this reduction in spar thickness was large enough to counteract the additional mass introduced by a larger number of vertical stiffeners, the stiffeners were assumed to be 5mm thick and run from the top to the bottom of the spar. This design is similar that seen in aircraft such as the A350 and A400M [13]. The mass of the unstiffened spar was found to be 845.3kg, whereas the optimally stiffened spar has a mass of 798.3kg, once the added mass of the stiffeners had been accounted for, justifying our choice of optimal stiffener placement.

One important aspect to consider is that there is now also shear flow in the skin, as well as the compressive loads from the bending moment. In order to assess whether this loading combination is satisfied by the structure, the following constraint can be checked against:

$$R_s^2 + R_c = \left(\frac{\sigma_c}{\sigma_{c,cr}} \right)^2 + \frac{\tau_s}{\tau_{s,cr}} \leq 0.99 \quad (19)$$

This was also implemented as a check in the optimisation code to ensure that this combined loading value never rose above 0.99 along the length of the wing. The final thickness distribution of the spar, along with the spanwise value of the combined loading are given in figure 21.

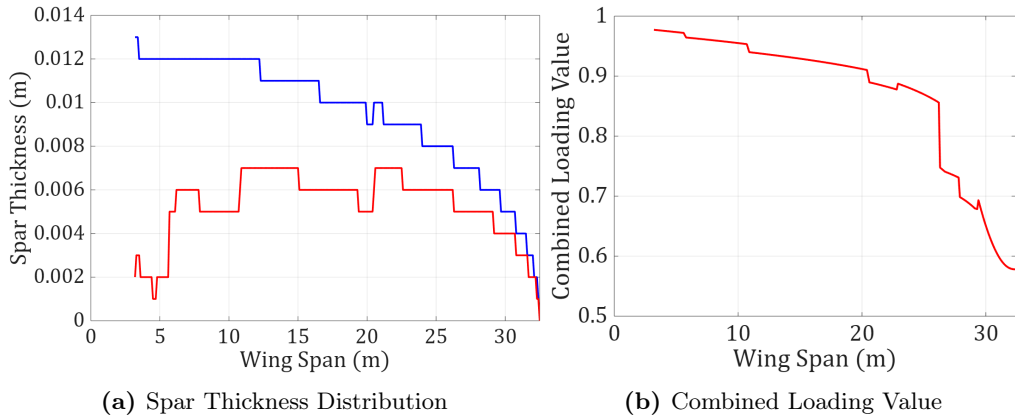


Figure 21: Spar Design Results

4.7 Ribs

Whilst we have considered methods to reduce the effective length of our skin panels in the chordwise direction, we are yet to apply the same method in the spanwise direction. This is the purpose of ribs. Ribs are able to withstand the crush load applied to it in the vertical (or radial) direction under the presence of a bending moment. The crushing stress can be equated to the buckling stress of the rib to enforce optimum material efficiency, and as such the rib thickness distribution was found from the following formula:

$$t_{\text{rib}} = \sqrt[3]{\frac{F_{\text{crush}} b_2}{3.62 E c}} \quad (20)$$

By inspecting the stresses applied to the rib due to the crush load, it was clear that the magnitudes are much lower than the yield stress, reaching at a maximum 50.9MPa. In order to save weight, circular cutouts can be used. These cutouts alter the stress field in the rib and concentrate stresses to particular points around the circular cutout. Due to the already low value of the stresses, this was deemed an acceptable trade-off. By selecting a cutout diameter to rib width ratio of $d/b=0.48$, the stress concentration rises to 339.7 MPa, having been scaled by a factor of 7.9, still below the yield stress of the material, and the shear buckling factor scaled by 0.47, to produce a new skin thickness distribution [7]. Due to the presence of these cutouts, the new rib weight is 677.7kg which is a saving of 178.2kg, down from 855.9kg without the cutouts.

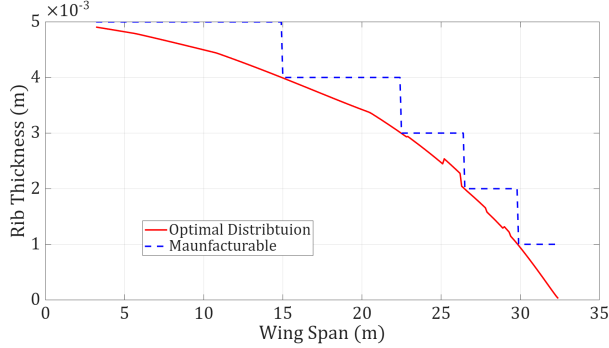


Figure 22: Rib Thickness Distribution

While possible to improve the buckling performance of the ribs by the addition of chordwise vertical stiffeners, the additional weight gain would counteract the cutouts and lead to a needlessly complex design from a manufacturing standpoint. From a structural view, there was also no failure criteria being met which means the addition of the hole does not necessitate any improved structural performance that might be seen due to the presence of the stiffeners. For these two reasons, it was decided that no stiffeners be added to the ribs.

4.8 Leading Edge Design

The leading edge of our wing heavily features actuating high lift devices, therefore was assumed to provide no contribution to carrying torsional load. Instead, the LE was sized to comply with bird strike and hail impact regulations. A minimum thickness of 1.6mm is required to negate damage from hail [8]. CS 25 dictates that the wing must withstand impact from a 8lbs bird at VCruise as sea level or 0.8 VCruise at 8000ft [1]. Using the impulse momentum equation, the impact force was approximated as 205kN, assuming an impact time of 5ms. The average Canada goose has a frontal width of 23.5cm [9], which when modelled as a circular object, exerts a stress of 4.7MPa on the LE. Thin pseudo ribs of 0.25mm thickness were used to stiffen the LE skin. The buckling stress with different numbers of pseudo ribs and skin thicknesses were determined and compared to the bird strike stress in Figure 23a. The weight of the LE section monotonically increases with skin thickness and rib number therefore it was important to minimise these. Figure 23b was used to determine the buckling stress per kilo of each combination. A final design of 24 pseudo ribs and 1.8mm thick skin with a buckling stress of 5.44MPa and total weight of 528kg was selected.

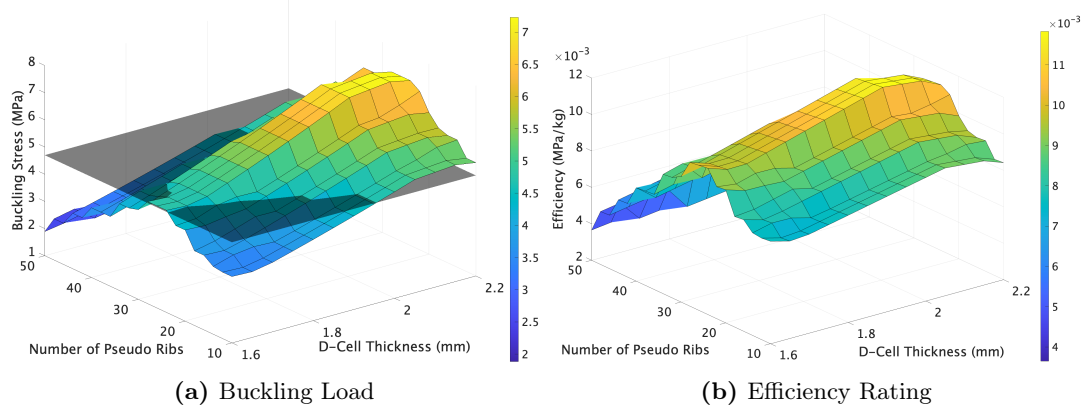


Figure 23: LE Sizing

5 Empenage

5.1 Horizontal Tailplane

5.1.1 Loading

Similar to the wing, all loading cases for the Horizontal tailplane were considered at load factors $n=-1.5$ and $n=3.75$ at V_a and V_D . The lift forces were computed by solving Equation (21).

$$M_{cg} = M_{0w} + (x_{cg} - x_w)(L - L_h) + (x_{cg} - x_h)L_h + l_t T \quad (21)$$

The horizontal tailplane's lift force was distributed elliptically over the horizontal tailplane using the following relation, where s is given as semi-span. All load cases were considered as seen in Figure 24a, with the most constraining case being with a load factor of -1.5 with the aircraft flying at V_D . Therefore, this was used as the basis of design.

$$L_h(y) = \frac{2L_h}{\pi s} \left(1 - \frac{y^2}{s^2}\right) \quad (22)$$

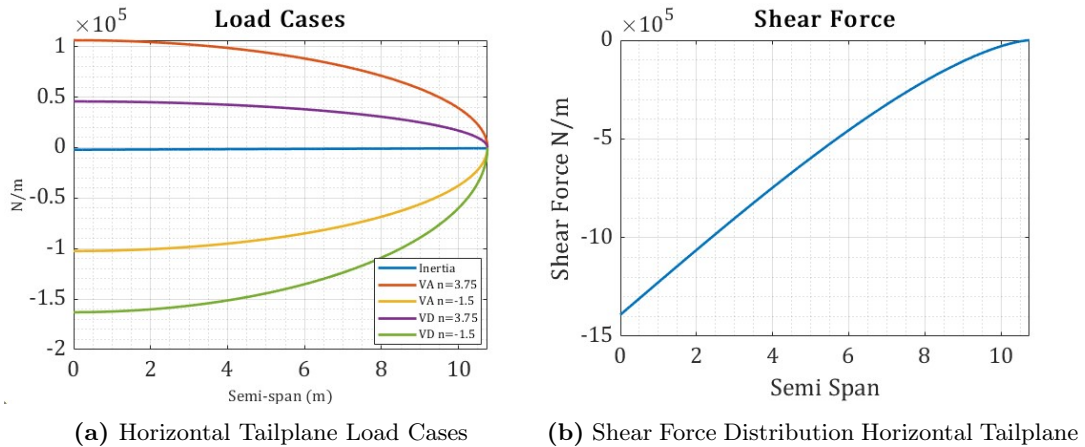


Figure 24: Horizontal Tailplane Loading

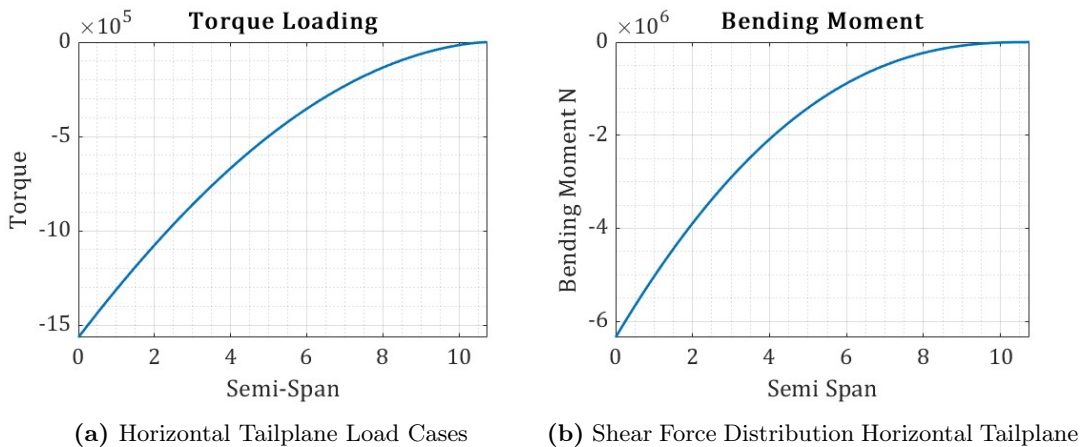


Figure 25: Horizontal Tailplane Loading

5.1.2 Skin and Stringers

The skin and stringer panels were sized to withstand the compressive axial forces. For structural efficiency the skin thickness was sized such that flexural buckling and local buckling happen at the same load. From the most constraining load case graph, our bottom panel would take higher compressive loads than the top skin panel. However, both were sized for the same maximum compressive load for a robust design that has lower complexity in production, maintenance and inspection. To begin stringer pitch was considered,

since that would directly affect the applied stress. Figure 26 clearly shows that for stringer pitch below 0.145 our design would fail under compression, therefore this was set as the lower bound for optimisation.

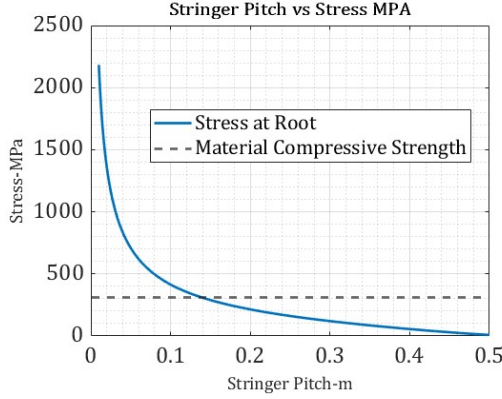


Figure 26: Stringer Pitch Limits

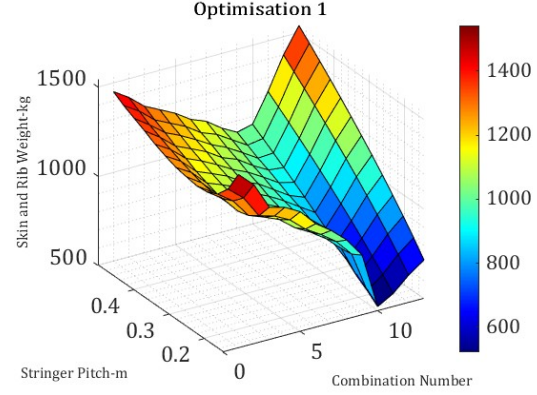
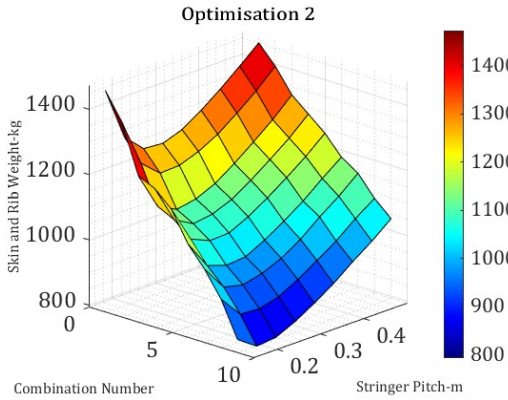


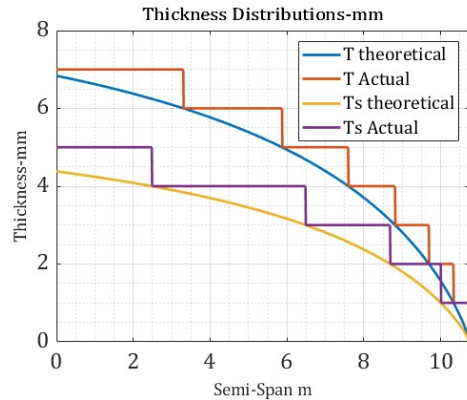
Figure 27: Second Optimisation

Z stringers were chosen because of their ease of manufacture, and their torsional rigidity [10] which is important due to the high torsional loads experienced by the horizontal tailplane. For our design the main variables to consider were the ratios $\frac{A_s}{bt}$ and $\frac{t_s}{t}$. Thus the values for these ratios that satisfy a farrar efficiency factor of 0.75 were chosen to ensure a farrar efficiency above 0.7 across our horizontal tailplane. 24 combinations were originally selected, along with 24 values for stringer pitch. The first optimisation results, shown in Figure 27, indicated to us that a value of A_s/bt as 0.48, t_s/t as 0.42 and b as 0.1 was the optimum minimum weight design for the skin and rib weight combined. This optimisation filtered out stringer geometries which would fail due to skin-buckling and torsional instability. The combination number on the x axis refers to the combination of A_s/bt and t_s/t . Another optimisation filter was run to see which designs satisfied skin-structural constraints such as the combined loading condition which meant that our σ/σ_{cr} ratio had to be less than 1. The result shown in Figure 28a, giving us our final design parameters of A_s/bt as 0.43 and t_s/t of 0.64 and b as 0.2.

Once our relevant design parameters were set, we computed our skin thickness and stringer area distributions. The calculated thickness distribution is not ideal for manufacturing constraints therefore our thickness was discretised as shown in Figure 28b. Upon Computing our skin thickness and stringer area distributions we analysed our stress-distributions to understand if they satisfied the relevant criterion. The compressive stress was less than the compressive yield stress as expected. As for the shear stress distribution, we computed the variation of applied shear stress, shear buckling stress and shear yield stress. The criteria that the combined loading of shear and compression on the skin that had to be satisfied was given by Equation (19).



(a) First Image



(b) Second Image

Figure 28: Second Optimisation and Final Thickness Distributions

Initially this criteria was not being satisfied. R_C was a constant chosen based on our optimisation and hence the selection of A_s/bt and t_s/t . We could decrease this, however this would increase t_s/t and A_s/bt

and hence also weight. A more feasible decision was to consider the shear stress ratio, R_S or σ_s/σ_{cr} . A way to decrease this would be to distribute torsional loads between both our wing box and the D-Cell, allowing us to maintain our chosen minimum weight design parameters for the skin-stringer panel. The initial shear model using just the wingbox was modified to get the idealisation shown in Figure 62, which splits the shear flows. Solving for q_1 (utilising the equations for twist and Torsional area equivalence), the shear stress on the skin with the D-cell included in our model was given along the span by Equation (23).

$$\tau_{skin} = \frac{q_1}{t_{skin}} \quad (23)$$

The Critical buckling shear stress was also computed. The smaller of critical shear buckling and shear yield stress was used as σ_{cr} to compute the R_S factor (σ_0/σ_{cr}). This was to ensure that our skin design was structurally robust and conservative to withstand the combined effects of shear and compression for both shear yielding and buckling cases. Figure 29 demonstrates how distributing torque loads between the wingbox and D-Cell improved the performance of our skin against combined loading. For our skin the maximum compressive and shear stress at the root were 184.81 MPa and 117.426 MPa, both of which were less than the compressive and shear strengths of Aluminium 2024 T3.

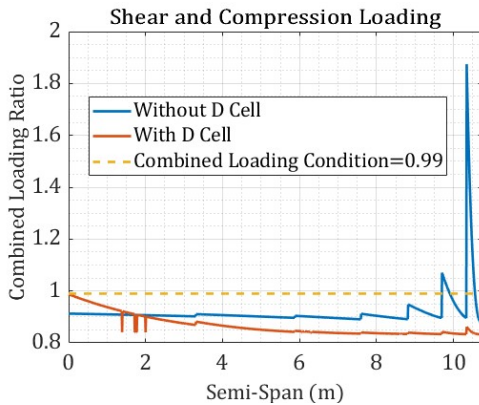


Figure 29: Compressive Stress Distribution

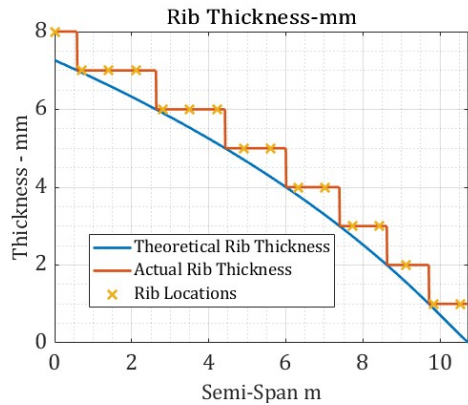


Figure 30: Rib Thickness Distribution

5.1.3 Ribs

The spacing for the ribs was computed using the farrar relation at every span configuration was given by Equation (24). N was the applied compressive load and σ_{cr} was computed using the $\frac{\sigma_{cr}}{\sigma_0}$ relation derived from the catchpole diagrams, based on our chosen stringer geometry. The rib spacing was computed for each of our combinations of As/bt , ts/t and b , using 24 and the optimised distribution was that which corresponded to minimum combined weight of the skin-stringer panels and ribs. The rib thickness distribution was computed using 20.

$$L = \frac{f^2 NE}{\sigma_{cr}^2} \quad (24)$$

5.1.4 Spars

The spars were sized to carry the shear load exerted on the wing. The shear flows due to torque were calculated, via the twist and torsional equivalence equations. The shear stress on the front spar were given by the following equations.

$$\tau_{front} = \frac{q_2 - q_1 - \frac{V}{2h_{front}}}{t_{front}} \quad \tau_{rear} = \frac{q_1 - \frac{V}{2h_{rear}}}{t_{rear}}$$

These stresses were equated to the shear buckling stress for each spar to solve for the thicknesses of the front and rear spars. The following thickness distribution was computed. When compared to the thickness distribution computed for the wingbox only taking the entire torsional loads, these thicknesses were lower, validating our decision to split the torsional between the wingbox and the D-Cell.

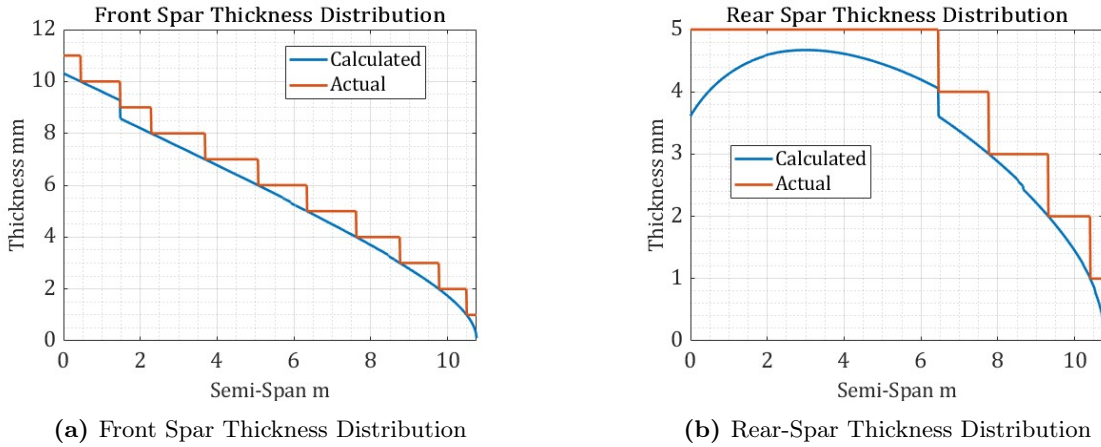


Figure 31: Spar Thickness Distributions

It is evident in the thickness distribution for the rear spar, that the calculated thickness starts off at 3.6 mm and increases until 4.5 mm close to 3 metres across the span, beyond which the thickness decreases until the tailplane tip. The decision was made to keep the thickness a constant 5 mm (instead of beginning at 4mm and increasing to 5mm) during the region where the calculated thickness increased. This was because discontinuities in thickness, such as thickness increasing and then decreasing again can create even further stress concentrations than there already are in the wing structure. Additionally there are reaction forces from the fuselage exerted on the spars, in the region close to the root. Therefore to mitigate these effects for a structurally robust design, the thickness of the spars started off at 5mm. For a final check we computed the shear stress distributions to verify that they did not exceed the shear yield stress of the material. Our maximum shear stress for the spars was 110 MPa at the root of the rear spar, which is below the shear yield strength of 310 MPa of Aluminium 2024 T-861.

5.1.5 D-Cell Design

Our idealisation for the wingbox which was split into a D-Cell and rectangular box allowed us to compute the shear flow and consequently the shear stress around the D-cell region. Therefore a decision was to be made to whether to size our D-Cell for the shear flow stress or whether the tresca yield stress of Aluminium 2024 T861. We computed our mass results for both. The panel thickness was found by solving for t in the equation below and equating buckling shear stress to our relevant critical shear stress. This critical shear stress was either q/t if considering shear flow or the tresca shear stress. K_S is a function of the D-cell geometry, number of panels and the panel thickness.

$$\tau = K_s E \left(\frac{t}{b} \right)^2 \quad (25)$$

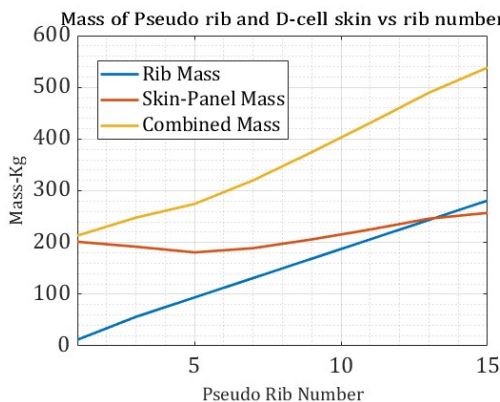


Figure 32: Mass Calculation for D-Cell-Sizing for shear flow stress

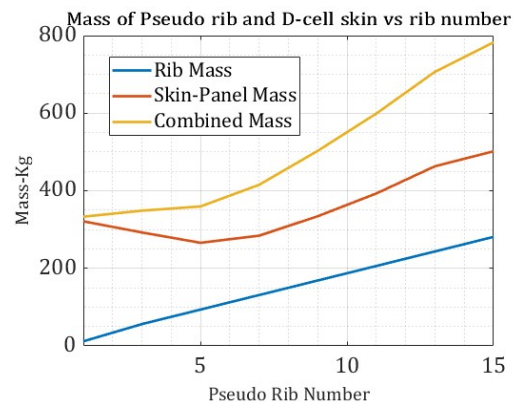


Figure 33: Mass Calculation for D-Cell-sizing for tresca shear stress

It is evident that sizing for shear flow stress gives us a lower mass. However this means that we will

have to check if our design satisfies the tresca shear requirement and potentially modify it if it does not. Additionally it is evident from both figures that the combined mass will increase monotonically with Psuedo-Rib Number. However for skin mass there is a mass that corresponds to a Psuedo-rib number of 5. The ideal solution would be to have zero Pseudo ribs which would give the lowest combined mass however from a structural point of view we want to include Pseudo-ribs to help maintain the aerodynamic shape of the aerofoil and transfer loads and stresses more evenly across the structure. Therefore as a compromise we will be choosing 5 Pseudo-ribs for our design, since 5 Psuedo-ribs give the lowest skin mass. The computed D-cell panel thickness variation and stress distribution in the D-Cell is shown below.

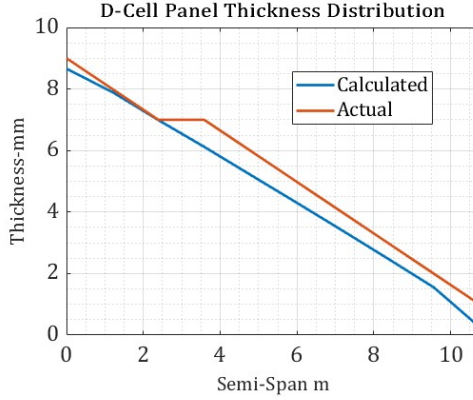


Figure 34: D-Cell Thickness Distribution

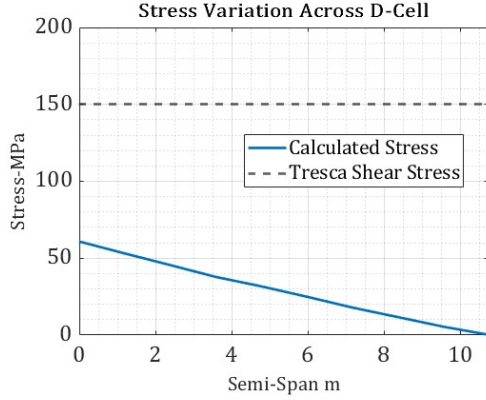


Figure 35: D-cell Stress Distribution

Our computed shear stress is below the tresca shear yield stress, indicating that our design is structurally feasible.

5.2 Vertical Tailplane

5.2.1 Loads

The relevant and critical loading case to size the Vertical tailplane would be the One Engine Inoperative OEI Load case, specifically when the outermost engine is inoperative. The lift force generated by the tailplane in this situation would be given by the following equation, in which x_e is the distance of the outermost engine's center of gravity from the aircraft's center of gravity and x_v is the vertical tailplane's aerodynamic center. Using the max lift force generated by the tailplane the shear, bending moment and torsional loads were computed.

$$L_{VT} = \frac{T_{max}(x_e - x_{cg})}{x_v - x_{cg}} \quad (26)$$

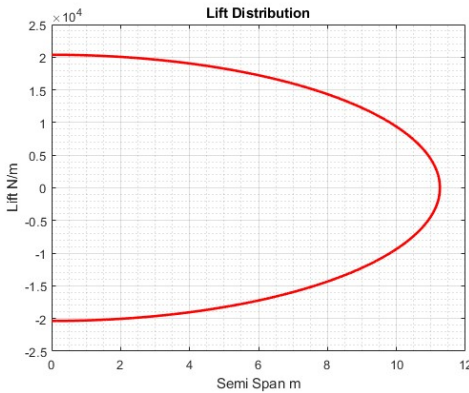


Figure 36: Lift Force Distribution

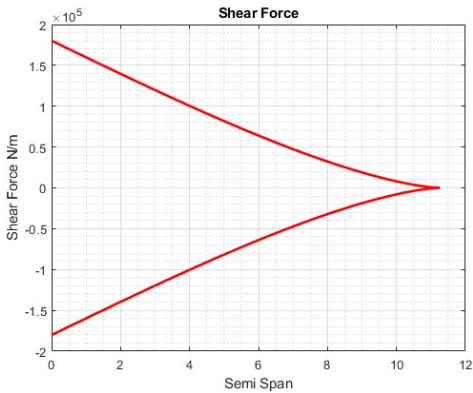


Figure 37: Shear Force Distribution

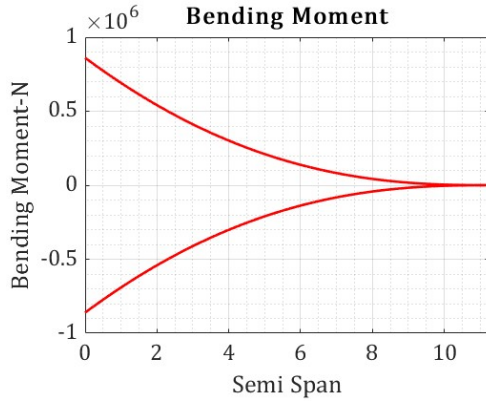


Figure 38: Bending Moment Distribution

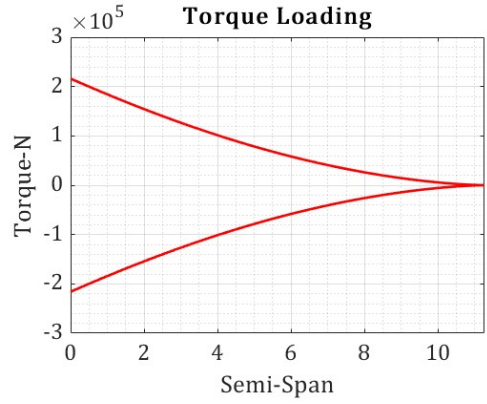


Figure 39: Torque Distribution

5.2.2 Composite Skin Covers

We sized our skin panel of the vertical tailplane to take the compression loads generated due to the bending moment. For compression loads, the number of 0 degrees plies were computed using equation 27.

$$n_0 = \frac{BM}{\sigma_c t_{ply}} \quad (27)$$

The Lockheed Martin rule was applied by which we computed the number of +/- 45 ° and 90 ° plies. The number of 45 and 90 degrees plies was 10% of the number of 0 degrees plies rounded to the nearest integer and multiplied by 2 since the number of plies had to be even. The number of plies computed was a constant value of 2 for the zero degree plies. However the initial values of the Ply Number for different angles had to be drastically changed to satisfy structural requirements. Two main structural criteria had to be satisfied by our skin cover design, which are outlined in the equations below, which dictate buckling ratio requirements for shear and compression as well as criteria for combined loading.

$$\frac{N_x}{N_{xb}} = < 1 \quad (28)$$

$$\left(\frac{N_{xy}}{N_{xyb}}\right)^2 + \frac{N_x}{N_{xb}} <= 0.99 \quad (29)$$

We aimed to size our ply's such that the direct buckling ratio in equation 28 was as close to 0.99 as possible, and then modify our layup only if 29 was not satisfied. Essentially we kept our design methodology for sizing the skin of the vertical tail similar to that of the Horizontal tail by taking compression as the primary criteria. This would ensure a design that satisfied structural requirements whilst being weight efficient. To begin designing our layup distribution the span of the Vertical tailplane was first discretised into 8 stations. The optimal layup for 8 total stations along the span was computed. The layup was then modified when the 8 were connected together in one continuous layup. This layup can be seen in the 40.

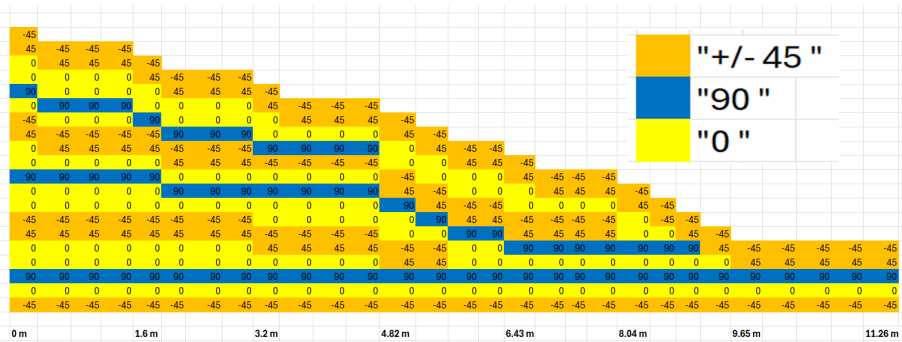


Figure 40: Skin Layup Distribution till Mid-plane

We ensured to follow standard and acceptable practices when completing the layup design. The laminate was ensured to be symmetric such that the total layup would consist of the layup shown in addition to

it's mirror image. There was an equal number of 45 and -45 degrees plies on each half of the total ply to ensure a balanced response to shear stresses in both directions in order to prevent warping and distortion. The midplane was made up of -45 degree plies to efficiently resist shear loads which are the highest near the mid-plane of the layup. We also took careful note to interleave the dropped off piles with continuous piles. In order to satisfy the stacking sequence 0 degrees piles were chosen to be stacked on top of one another to continue their sequences. This maximises stiffness and strength in the 0 degrees direction which is beneficial for compression loading. The stress ratios for our layup is given as follows:

Table 9: Compressive Stress and Combined Loading Ratios for Skin Layup

Span (m)	0	1.6	3.2	4.82	6.43	8.04	9.65	11.26
Nx/Nxb	0.8634	0.8628	0.8936	0.8166	0.9276	0.7475	0.8072	0
$Rs^2 + Rc$	0.8724	0.8730	0.9074	0.8344	0.9624	0.7875	0.9230	0

5.2.3 Composite Spars

To size our composite spars to carry the shear force the vertical tailplane experienced we first calculated the loading on the front and rear spars which were given by the following equations.

$$SF_{front} = \frac{V}{2h} + \frac{T}{2A_{box}} \quad SF_{rear} = \frac{V}{2h} - \frac{T}{2A_{box}} \quad (30)$$

Since the loading being considered is shear loading an initial calculation was undertaken to compute the number of 45/-45 degree plies across the span using the following equation.

$$n_{45} = \frac{SF_{front/rear}}{t_{ply} \sigma_{shear}} \quad (31)$$

The variation of ply number as seen in 41 and 42 was computed. The computed number of 45 degree piles was rounded up and multiplied by 2 since there had to be the same number of -45 and 45 degree plies. The number of 0 and 90 degree plies was 10% of the number of -45/45 degree plies multiplied by 2 to satisfy symmetry requirements. These initial ply distributions were modified to satisfy shear buckling requirements and minimise mass. The same standard practices which we adopted to complete our Skin layup were used for our spar layups. The stress ratios for the front and rear spars are given in Table ??, and their layups are presented in 43 and 44.

Table 10: Shear Stress Ratios for Rear Spar Layup

Span (m)	0	1.6	3.2	4.82	6.43	8.04	9.65	11.26
Nxy/Nxy_b Front	0.9811	0.9079	0.9430	0.9839	0.8683	0.8879	0.7705	0
Nxy/Nxy_b Rear	0.8735	0.8731	0.9234	0.9563	0.8857	0.8465	0.8106	0

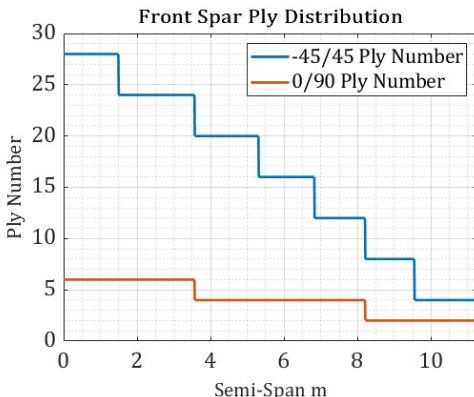


Figure 41: Front Spar Ply Distribution

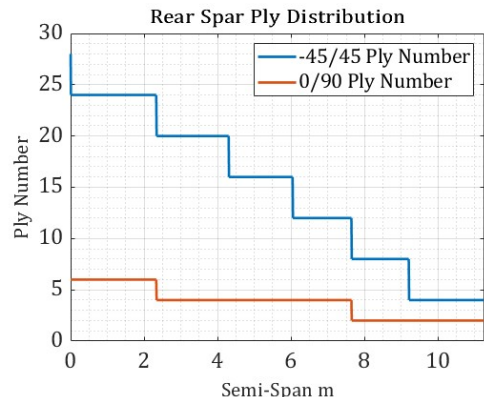


Figure 42: Rear Spar Ply Distribution

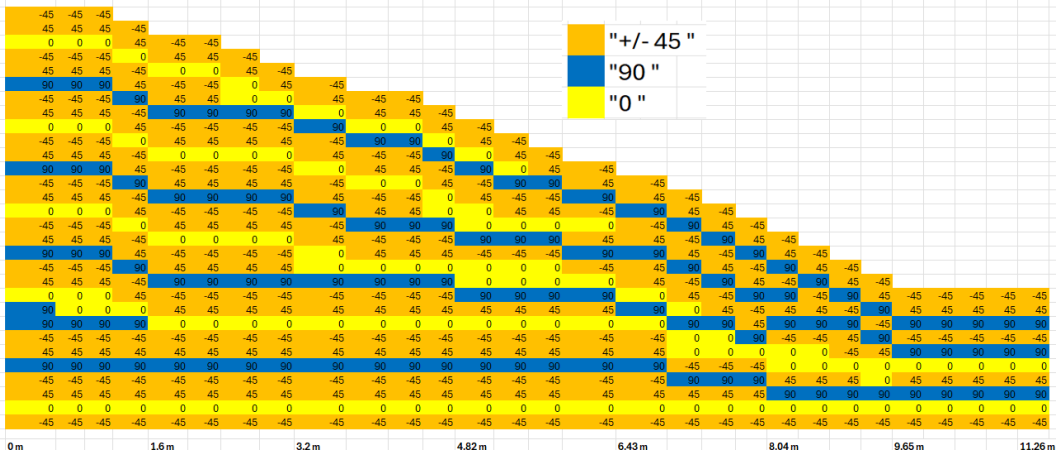


Figure 43: Front Spar Layup till Midplane

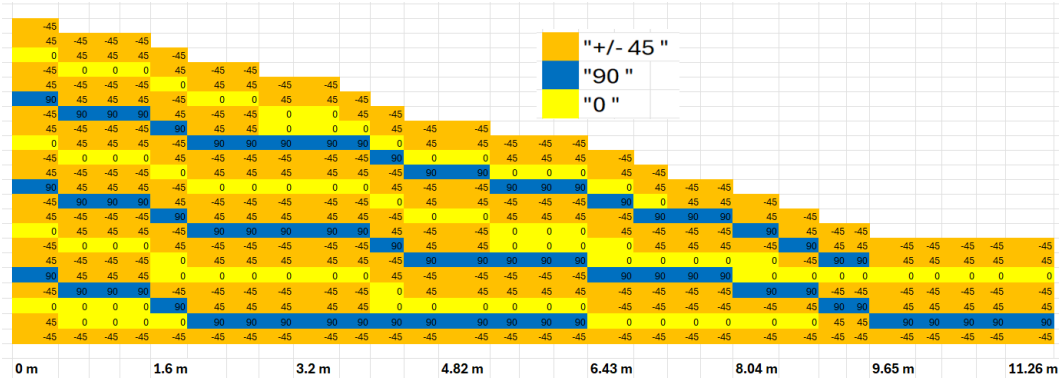


Figure 44: Rear Spar Layup till Midplane

5.2.4 Composite Ribs

To compute the composite rib layup we calculated our crush force at each rib location via the same formula used to compute our rib thickness for the horizontal tail. This was taken as our applied load or N_x , which was computed using the formula for crush load in the wing. The Young's Modulus for each layup was calculated based on elements of the A matrix, the equation for which is given by 35 from [21]. To calculate our critical buckling load N_{xb} we made use of the following formula:

$$N_{xb} = \frac{K_o(D_{11}D_{22})^{1/2}}{b^2} + \frac{2\pi^2}{b^2}(D_{12} + 2D_{33}) \quad (32)$$

K_o was computed based on the geometry of our rib which included rib width and rib height. We did not take the same formula for N_{xb} which we used for our composite skin. This was because for the skin geometry which in which the width was stringer pitch and the length was the rib spacing our K_o value went asymptotically to 19.7 or $2\pi^2$. However for the rib geometry, the rib depth or length was smaller than rib width. So our (a/b) or length/width ratio was less than 3.0. Therefore the EDSU 80023 was used to interpolate and compute K_o for each value of $\frac{a}{b}(\frac{D_{22}}{D_{11}})^{1/4}$ based on our rib geometry and the layup for the rib. We once again began by computing the number of plies by dividing our crush load per unit metre with the product of ply thickness and ply strength. The layup was then modified to satisfy axial buckling requirements. The layups are shown in Table 11.

5.2.5 D-Cell

For the D-cell of our vertical tailplane a metallic design was considered because of complexity in manufacturing a composite layup for the curved leading edge shape of our wing. Problems can arise such as fibers misaligning and wrinkling, inconsistencies in the resin distribution, uneven curing and tooling complexity for molds. To size our D-Cell we equated our buckling stress to the critical load which in this case was the stress exerted due to a bird strike impact. We did not consider torsional and shear loads since the wingbox was sized to take the full torsional load at each span point. Similar to for the horizontal tailplane

Table 11: Rib Composite Layups

Rib No.	Layup	Nx/Nxb
1	(-45/45/0 ₂ /90/0/0/-45/45/0 ₂ /90/-45/45/0 ₂ /90/0 ₂ /-45/45/90/0/-45) _s	0.9541
2	(-45/45/0 ₂ /90/0 ₂ /-45/45/0/0/90/-45/45/0/90/0/-45/45/0/-45) _s	0.9833
3	(-45/0/45/0/90/0 ₂ /-45/45/0 ₂ /90/0/-45/45/90/0 ₂ /-45) _s	0.8737
4	(-45/0/45/0/90/0 ₂ /-45/45/0 ₂ /90/0 ₂ /-45) _s	0.9204
5	(-45/0/45/0/90/0 ₂ /90/0 ₂ /90/-45) _s	0.8076
6	(-45/0/45/0/90/0/90/-45) _s	0.7866
7	(-45/45/0/90/-45) _s	0.2185

Table 12: Mass Calculation for Vertical Tailplane

VT Component	Mass (Kg)	HT Component	Mass (Kg)
Skin and Stringers	106.43	Skin and Stringers	483
Ribs	73.81	Ribs	310
Front Spar	79.78	Front Spar	154.2
Rear Spar	26.54	Rear Spar	57.4
D-Cell Panel	220	D-cell Panel	185
Weight	506.56	Weight (1 side)	1189.6
-	-	Weight(total)	2379

we iterated through different Pseudo-rib numbers and chose the configuration which resulted in the lowest mass. Based on our optimisation, 3 Pseudo ribs were chosen for our vertical tailplane. The D-cell panel thickness distribution is computed below. Once again combined mass increased Monotonically, however there was a minimum for skin mass which corresponded to 3 Psuedo-ribs. Therefore 3 ribs were chosen.

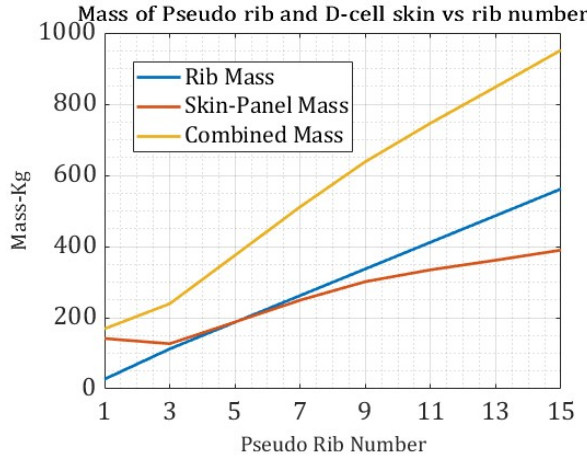


Figure 45: Mass variation with Psuedo-rib Number

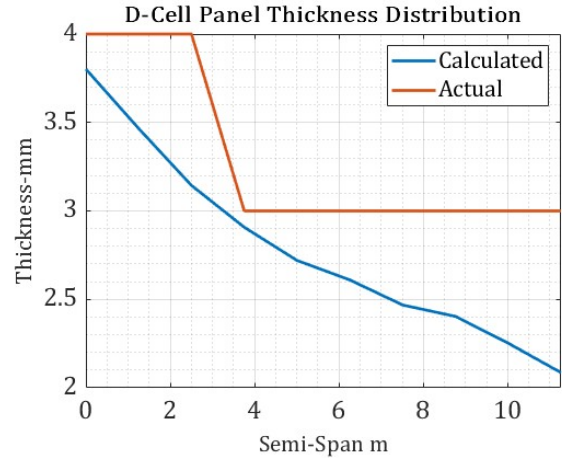


Figure 46: D-Cell Thickness Distribution

5.3 Mass Calculation

The mass breakdown for our vertical and horizontal tailplane is given as follows

6 Fatigue analysis

Our aircraft is a long range high capacity jet targeted for use in long haul flights. Therefore it expected use will be one ground-air-ground cycle per day based on the current usage of similar sized aircraft like the A350, A380 and 777 by airlines. These aircraft are also certified for around 25-35 years with lifespans ranging from 30,000 flight cycles to 60,000.

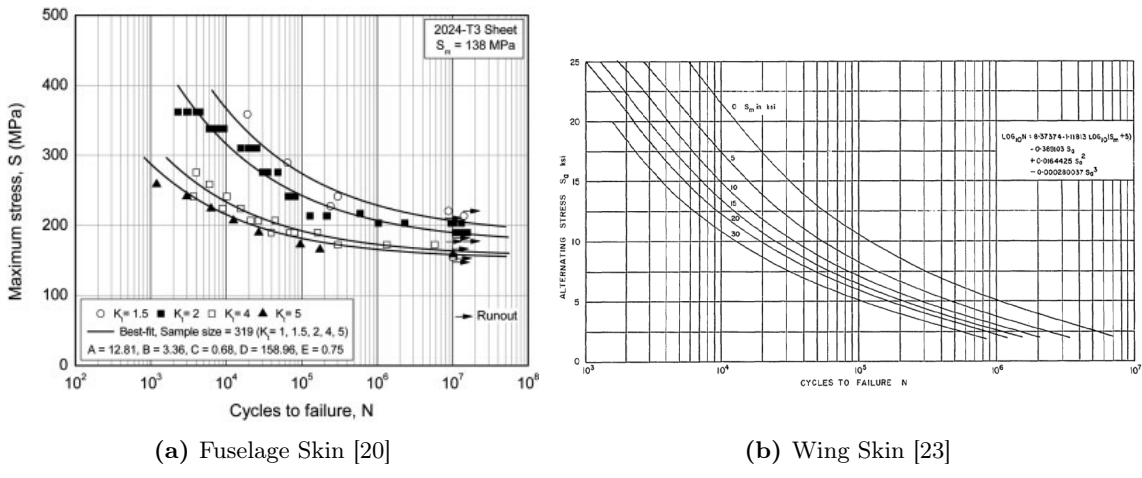


Figure 47: Al 2024 T3 S-N Curves for Fuselage and Wing

The fuselage skin experiences cyclical stresses from the repeated pressurization cycles each time it flies. To investigate the cycle limit of the fuselage, we used Basquin's Law using $N_f = (\sigma_f/\sigma_{\text{hoop}})^m$. With the hoop stress having been calculated previously in the fuselage section at 17.50 MPa and reading the fatigue stress from the S-N curve at 138 MPa with $m=5$, the number of fatigue cycles is 30454. This is in line with expectations for an aircraft of our specification.

For the wing, the largest stress seen at the manoeuvring limit of $3.75g$ is 281 MPa. Assuming a linear relation between the load factor and the stress, the maximum stress experienced at $1g$ level flight is 74.4 MPa. To produce a more realistic ground-air-ground (GAG) loading cycle, real world flight data from a Boeing 737-400 was used [22]. This data is more likely to be representative of the loads experienced by our aircraft, and is an improvement upon the data given by the FAA for smaller aircraft [19]. With knowledge of the alternating and mean stresses for each stage of the GAG cycle, it is possible to use the S-N diagram for Al-2024 given in figure 47b to find the number of cycles until failure. The total damage for one 400 hour flight block was found to be 0.00060, leading to a total of 33827 fatigue cycles. This value is achieved with a scatter factor of 4.95, which was calculated according to equation 4 of [19].

7 Secondary Components

7.1 Joints and Fittings

One major design decision to be made for Joints and Fittings was to decide what wing root joints to use. There were 4 options to be considered which consist of Tension bolts, Lugs, Splice plates and lastly a combination of splice plates and tension bolts. Lugs were discarded because of them being more economic for military aircraft with thinner aerofoil. We will be using Splice plates rather than tension bolts for our wing root joints, since they are more effective in reducing stress concentrations at the root, since the plates transfer loads over a larger area. Additionally the overlapping design of splice plates helps counter crack propagation, an example of their robust resistance to fatigue. Splice Plates are also secured with multiple fasteners, which is an important safety feature especially in the scenario when fasteners fail.

7.2 Cutouts

In the fuselage, large cutouts will be needed for passenger doors and cargo bay doors with smaller cutouts scattered around the structure for access to joints, fittings, Electric and Hydraulic systems and windows. The primary effect of cutouts are the introduction of stress concentrations. The effect of smaller/medium cutouts is localised so the redistribution of mass to reduce the stress concentrations can be done relatively easily and locally[lecture ref]. The windows are typically placed on a single skin panel and do not cut through any stringers or spars so to reduce stress concentrations the windows only need local reinforcement. To reduce these stress concentrations the window corners will use doubler plates and the corners will be rounded off significantly making them effectively ovals.

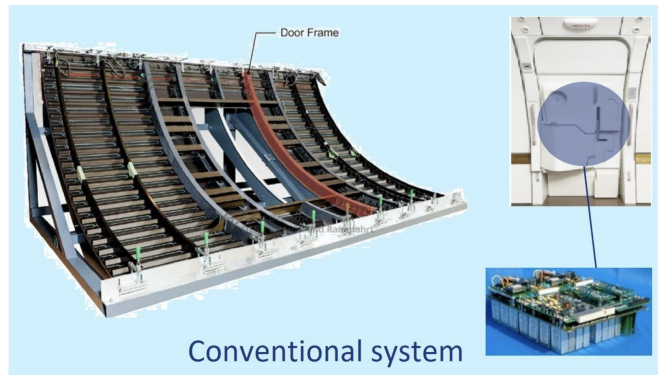


Figure 48: Structural super capacitor C section beams [Emile]

Passenger and cargo doors will need a door-surround-structure (DSS) for reinforcement to redistribute the high forces acting in the fuselage due to the applied internal pressure and the flight loads around the cut-out. High biaxial tensile loads arise from the internal pressure similar to a pressure vessel. Shear, compression, and tension loads result from flight manoeuvres and lift. Conventional door surround structures are composed of two metallic components: doubler plates and edge reinforcements and will be used for the main passenger and cargo doors. The doubler plates will be used in the corners to withstand the shear forces and edge reinforcements include all actual parts of the frame structure (intercostals, edge frame, sill and lintel). The main function of the edge reinforcements is to redistribute the forces (bending, hoop and shear loads) around the door cutout[get a diff ref]. For the smaller doors on the wing since they are 'plugged'(door sealing is achieved via cabin pressure) a novel integral thermoplastic DSS as described in [3].

This provides a significant mass saving benefit[same ref]. By incorporating a novel structural supercapacitor for one or 2 of the door frame C-section beams a potential mass saving of 4.2 KG per door can be achieved. The electrical systems for the larger normal passenger doors use a bulky bank of supercapacitors [Emile structural power imperial] that are normally located on the door which can now be replaced with power from the C section beams⁴⁸.

7.3 Engine mounts

Due to wide use in industry and reliability, we will be using pylon mounts for our engines. We will be utilising a patented aircraft engine fail safe engine mounting system [11]. This system is well suited for engines with thrust reversers such as ours. The system for connecting an aircraft engine to the aircraft consists of a primary mount component featuring a fail-safe clevis as well as a secondary mount component which consists of a second fail-safe clevis. The second mount component includes a body element, an engine casing equipped with a lug and casing clevises, and a single-piece thrust link that connects the body element to a section of the airframe. This thrust link is designed to transmit engine thrust loads to the aircraft structure.

8 Detailed Design

8.1 Objectives and Setup

After completing our preliminary design, we moved on to designing the detailed component design part of the brief, where we were required to design a flap mechanism. The designed flap mechanism must withstand a limit load of 7.5 kN and not deflect more than 2.2 mm (deflection in line with the force applied). In line with industry standards, a safety factor of 1.5 should be set giving the Ultimate Load to be carried by the structure should be 11250 N . Fatigue was not considered as the testing for this project did not involve extended cyclic loading. The major modes of failure of the structure being designed are expected to be tensile failure and buckling. The brief also outlines a performance index to be maximised below. To remain competitive we aimed for a performance index between 35 and 45 at the ultimate load, which meant our design would be between 250 and 325 grams.

$$\eta = \frac{LOAD}{MASS} \quad (33)$$

The component is to be milled from a 6.3 mm block of 6061-T6 aluminium alloy, whose properties have been highlighted in Table 13

E	ν	σ_y	σ_{UTS}	ρ
68.9 GPa	0.33	276 MPa	310 MPa	2703 kg m ⁻³

Table 13: Caption: Properties of 6061-T6 Aluminium Alloy [12]

Various sources list the yield stress of 6061-T6 Aluminium Alloy as 262 MPa; however, that is true when the material is being operated at 100° C; however, the yield stress of the material at room temperature is 276 MPa

8.2 Design Process

During the design process, ABAQUS CAE was used for the simulations for static and buckling analysis, as well as topology optimisation. We did not perform the topology optimisation on the blank provided to us initially, as this would be very computationally expensive as it would require a very large number of mesh elements a lot of material to be removed during the optimisation to achieve our volume target. While we could have gone for a very aggressive volume reduction during the optimisation process, we did not do this as the TOSCA topology optimisation tool does not optimise the blank for buckling. Instead, our designs began by analysing the behaviour of the blank under the constraints and loading conditions provided by running a linear static and buckling analysis, allowing us to identify areas of lower stress in the material that did not play a major role in preventing the structural element from buckling, or yielding such as can be seen in Figure 49

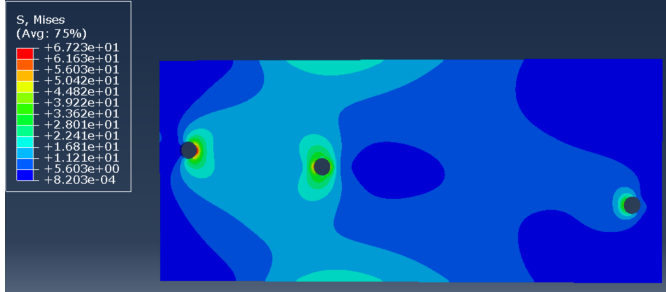


Figure 49: Plot of Stress Distribution in raw Blank

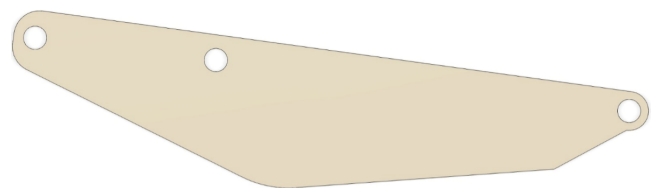


Figure 50: Modified Blank

To simplify our analysis, we only considered the bottom half of the blank with the corners of the blanks removed as shown in Figure 50 consistent with figure given above which clearly show that none of the corners of the blank actually carry any significant stress. Choosing the bottom half of the blank allows us to consider buckling due to direct compression, rather than due to the compressive forces arising due to bending in the upper half of the blank (By inspection it is clear that during loading, the upper surface of the blank would be bent in compression).

The topology optimisation was run in ABAQUS on the modified blank, with a weight of 1,243 grams, with the following loading and boundary conditions:

- A fully pinned boundary condition applied to the left-most hole, enforced at the centre of the hole.
- A pinned boundary condition applied to the right-most hole, enforced at the centre of the hole.
- The ultimate load of 11250 N acting downward from the middle hole, enforced at the centre of the hole. For our initial analysis, we also enforced no out-of-plane rotations.

All three conditions were enforced using a coupling constraint. While an MPC-Beam constraint was considered, this would not allow the holes to deform, which is not the case. The topology optimisation setup in ABAQUS is quite basic, as it only allows optimisation for a static loading case. The optimisation

was done to minimise the Strain Energy, while constraining the volume fraction to 30% of the initial volume of the modified blank. A circular area of diameter 30 mm around each of the loaded and constrained holes was frozen, and not removed during the optimisation as per the requirements of the brief. We used a refined version of our optimised modified blank as our first iteration as shown below.

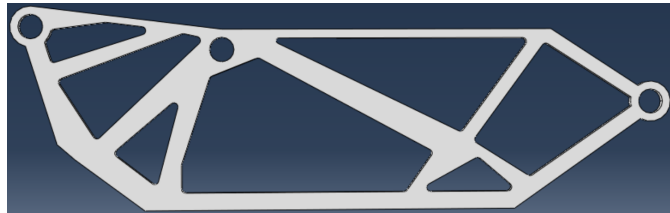


Figure 51: Iteration 1 of Detailed Component Obtained from Topology Optimisation

Running a linear static and buckling analysis according to the loading and boundary conditions mentioned earlier, we obtain values for the maximum force the structure can withhold before tensile or buckling failure, which allows us to calculate the merit index for this iteration. The table below highlight the performance of the first iteration.

Mass	Maximum Stress at Ultimate Load	Maximum Force for Buckling	Deflection	η
374 g	260.2 N	18000 N	1.6 mm	30.08

Table 14: Performance of Iteration 1

The merit index achieved by us for this iteration is 30.08. This is good progress considering this is a very basic iteration received from Topology Optimisation; however, our next iterations will focus on reducing mass to increase our merit index. We used the structure given to us by the optimisation to create a similar arrangement making use of the load paths exhibited by FEA, which has a lower mass and similar characteristics.

While creating this new truss structure, we encountered various issues. In sharp corners, there would be regions of stress concentrations that would go above our yield stress and reduce the buckling load. We solved these problems by experimenting with various fillet radii and thickening of truss members using the FEA stress distributions and buckling modes to identify the load paths. For the next 2 iterations, more material was added in that direction to assist the transfer of load. Iteration 4 was the first iteration where we were able to stay under the yield stress at all points whilst exhibiting good buckling characteristics (safety factor >1.5 at UTL).



Figure 52: Iteration 2 - Yields at Spar Joints



Figure 53: Iteration 4- Does Not Yield

Mass	Maximum Stress at Ultimate Load	Maximum Force for Buckling	Deflection	η
306.2 g	11,250 N	16,875 N	1.8 mm	36.74

Table 15: Performance of Iteration 4

After Iteration 4, we focussed on removing redundant mass from the structure without affecting its performance in buckling and yielding. The iterative design process was manual, and done in a manner as to save as much weight as possible from Iteration 4 to the final design. To reduce mass, we decided on an acceptable safety factor of 1.25 at the Ultimate Load, down from the 1.5 we had for iteration 4. This allowed us to reduce the thickness of the truss elements along the top surface of the component, saving approximately 35 grams in weight. We also made sure any redundant material was removed in the form of circular and elliptical ovals. The iteration is shown in the figure below, along with its performance metrics.



Figure 54: Final Design of Component

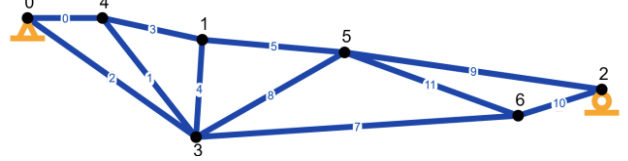


Figure 55: Pin-Joint Idealisation of Final Design

Mass	Maximum Stress at Ultimate Load	Buckling Failure Force	Deflection	η
269.8 g	274.4 MPa	14,261 N	2.01 mm	41.7

Table 16: Performance of Final Design

After this, a non-linear buckling analysis was run using the Static Riks step in ABAQUS by taking a small multiple of 0.4 of the deformation during the linear buckling for the first mode. The value of the failure load for the non-linear buckling case was calculated to be 12821.2 N. By comparing the various modes of failure, we expect the component to fail by out-of-plane non-linear buckling.

8.3 Pin-Joint Framework Analysis

To verify our FEA solver findings, we did a pin-joint framework analysis. It was found that that the members 0,3,5,9 and 4 in Figure 55 were all in compression, and member 5 had the chance for buckling, and no elements were close to yielding. This is concurrent with our findings with the FEA solver, as the only locations which are close to the yield stress in our final design, are the one near sharp corners, something that is not present in a pin-joint framework analysis.

We could; however, do a Euler Buckling Analysis on member 5 using the equation

$$P_{cr} = \frac{\pi^2 EI}{(KL)^2} \quad (34)$$

Where $K = 0.9$, higher than the K value of 0.5 for a fixed-fixed boundary condition which is what is imposed on the member in real life to account for eccentricity (load not being applied directly at the centroid, which could not be modelled for an analysis on paper; hence, this idealisation models for any problems that may arise due to a real-world scenario).

The Euler Buckling Load that was found was 15.09 kN by using the smaller moment of inertia of the face on which the load was applied, and the load in the member from the pin-joint framework was 14.42 kN, giving a safety factor of 1.046 on the ultimate load. Even though this is not as large as the safety factor for our FEA results, it is still reassuring since we have taken into account eccentricity, which decrease the euler buckling load for the member.

8.4 Grid independence

Finite element software discretises the model geometry and thus the level of discretisation affects the results. Increasing the number of elements generated will increase the accuracy and so a mesh convergence study must be conducted. This was conducted mathematically using the grid convergence index(GCI) following the methodology in [18]. If the Convergence parameter($\frac{GCI_{2-3}}{r^p * GCI_{1-2}}$) is close to one it can be established if the results have converged at the smallest mesh size. Our refinement ratio r is set at 2 and p is the order of convergence found using a Richardson extrapolation As can be seen in 17 the results for iteration 2 are very close but not fully converged at a mesh size of 1.5mm but this is the smallest size we could achieve with the license we are provided with ABAQUS CAE (250,000 elements max). Thus for all of our iterations a mesh size of 1.5 mm was used.

Mesh fineness	Element size mm	Maximum stress Mpa	GCI
Coarse(3)	6.000	120.0	N/A for mesh 1
Medium(2)	3.000	294.0	4.3517%
Fine(1)	1.500	306.0	0.2860%
			Convergence param = 0.8452

Table 17: Grid convergence study

9 Discussion

Considering the horizontal tailplane design, although optimisation was carried out, more combinations of the parameters As/bt and ts/t could have been iterated through for an even further minimum weight design. The final weight of our horizontal tailplane (2379 Kg) is similar to what we predicted in the conceptual design stage (2998 Kg). This does validate the accuracy of our structural calculations. Granted, our weight could have been even further lower, however given the high order of magnitude of the torsional and shear loads (10^5), the fact that our calculated weight is still less than what we predicted is acceptable. For further iterations we can ease some of the simplifications we made for our design process such as keeping Farrar efficiency constant across the span and keeping stringer pitch constant, which would allow us to iterate through more combinations.

For the design of our vertical tailplane, specifically the layups of the skin and spars across the span, we discretised our span into 8 stations, created the layups for each station and then connected the layups as shown in Figures 40, 43 and 44. For further design iterations the discretisations could be made even smaller, with the layup plan across the span being larger to ensure that as many sections of the skin and spars across the span are weight efficient whilst satisfying the criteria for compressive and shear buckling.

For the detailed component design of the flap extension mechanism, the process of taking out redundant material from the structure was manual after the first optimisation, as there were licensing problems with the software; however, this allowed us to more finely optimise the component to exactly to the performance metrics that we wanted. From our first iteration, which was obtained from the topology optimisation done in TOSCA, we increased our merit index from 30.08, to 41.7, reaching the target we set before starting the design process. In simulations, and analytical results, our detailed design had a safety factor of 1.87 on the Limit Load, and does not yield at the limit load, or the ultimate load. Further reductions in mass could have been made with a using a different initial blank that more closely aligned with the contour plot of the raw blank.

References

- [1] EASA. Certification Specifications for Large Aeroplanes [Internet]. Sep 19, 2007. Available from: <https://www.easa.europa.eu/en/document-library/certification-specifications/group/cs-25-large-aeroplanes>
- [2] Group 10. Conceptual Design Report. Imperial College London. 2024.
- [3] Jannis Philipp Hüppauff, Nagaraj V, Motsch-Eichmann N. DEVELOPMENT OF AN INNOVATIVE THERMOPLASTIC DOOR- SURROUND-STRUCTURE FOR A SINGLE AISLE-AIRCRAFT. SAMPE Europe Conference 2023 Madrid - Spain [Internet]. 2023 Oct 5;
- [4] Farrar, D.J. (1949). The Design of Compression Structures for Minimum Weight. Journal of the Royal Aeronautical Society, 53(467), pp.1041–1052. doi:<https://doi.org/10.1017/s0368393100120747>.
- [5] ESDU 71014: Local buckling of compression panels with flanged stringers [Accessed February 2025]
- [6] ESDU 71005: ESDU 71005 Buckling of flat plates in shear.[Accessed February 2025]
- [7] ESDU 75034: Initial buckling stress, maximum direct stress and shear strain of square plates in shear with central circular holes.[Accessed February 2025]
- [8] Niu MCY. Airframe Structural Design: Practical Design Information and Data on Aircraft Structures. : Adaso Adastra Engineering Center; 1999.
- [9] Dimensions.com. Canada Goose (Branta canadensis). <https://www.dimensions.com/element/canada-goose-branta-canadensis>: .text=The%20Canada%20Goose%20has%20a,(37%2D55%20cm).
- [10] Wu M, V RS, Wilson D. Design and testing of z-shaped stringer-stiffened compression panels – Evaluation of ARALL, GLARE, AND 2090 materials [Internet]. Osti.gov. American Society for Testing and Materials, West Conshohocken, PA (United States); 1997 [cited 2025 Feb 28]. Available from: <https://www.osti.gov/biblio/566535>
- [11] Alan Manteiga, J. Fail Safe Aircraft Engine Mounting System [Internet]. 2005 [cited 2024 Mar 28]. Available from: <https://patentimages.storage.googleapis.com/a0/4b/f4/db233b96026b60/US6843449.pdf>
- [12] <https://www.matweb.com/search/datasheet.aspx?MatGUID=b8d536e0b9b54bd7b69e4124d8f1d20a&c1>
- [13] Griffiths, B. (2013). A350 & A400M Wing spars: a Study in Contrasts. [online] www.compositesworld.com. Available at: <https://www.compositesworld.com/articles/a350-a400m-wing-spars-a-study-in-contrasts> [Accessed Feb. 2025].
- [14] Levis, E. (2022) Introduction To Aerospace AERO40002 Lecture Notes. [Accessed February 2025]
- [15] Wu M, et al. Design and testing of Z-shaped stringer-stiffened compression panels—Evaluation of ARALL, GLARE, and 2090 materials. 1997 Dec.
- [16] Imperial College London, Department of Aeronautics. WS3_Fuselage_Design [Excel spreadsheet]. 2024.
- [17] Hiken, A. (2017). The Evolution of the Composite Fuselage - A Manufacturing Perspective. SAE International Journal of Aerospace, 10(2), pp.77–91. doi:<https://doi.org/10.4271/2017-01-2154>.
- [18] Establishing Grid Convergence [Internet]. 2017 [cited 2024 Feb 9]. Available from: <https://curiosityfluids.com/2016/09/09/establishinggrid-convergence/>
- [19] Federal Aviation Authority (2005). Fatigue, fail-safe, and Damage Tolerance Evaluation of Metallic Structure for normal, utility, acrobatic, and Commuter Category Airplanes. [online] Available at: <https://www.faa.gov/documentLibrary/media/AdvisoryCircular/AC23-13A.pdf> [Accessed 28 Feb. 2025].

- [20] Al-Rubaie KS. A general model for stress-life fatigue prediction. [Internet]. Jun 2008. Available from: https://www.researchgate.net/publication/247989167_A_general_model_for_stress-life_fatigue_prediction [accessed 1 Mar 2025].
- [21] 1.Nettles A. Basic Mechanics of Laminated Composite Plates BASIC MECHANICS OF LAMINATED COMPOSITE PLATES (NASA. Marshall Space Flight Center) [Internet]. 1994. Available from: <https://ntrs.nasa.gov/api/citations/19950009349/downloads/19950009349.pdf>
- [22] D. Skinn (1996). Flight Loads Data for a Boeing 737-400 in Commercial Operation. U.S. Department of Transportation Federal Aviation Administration.
- [23] Professor Lorenzo Iannucci. Airframe Design Fatigue Design. Imperial College London

A Appendix A - Wing

A Appendix C - Empennage

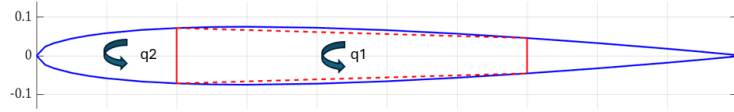


Figure 56: Wingbox and D-Cell Idealisation for Horizontal Tailplane

$$E_x = \frac{A_{11}}{h} + \frac{A_{12}}{h} \left(\frac{A_{26}A_{16} - A_{12}A_{66}}{A_{22}A_{66} - A_{26}^2} \right) + \frac{A_{16}}{h} \left(\frac{-A_{16}}{A_{66}} + \frac{A_{26}A_{12}A_{66} - A_{26}^2A_{16}}{A_{22}A_{66} - A_{26}^2A_{66}} \right), \quad (35)$$

A Appendix C - Detailed design

Figure 57: Iteration 1 results

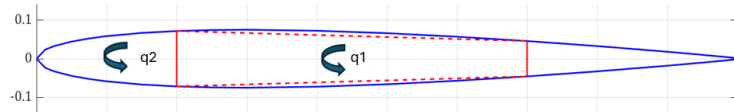


Figure 58: Iteration 2 results

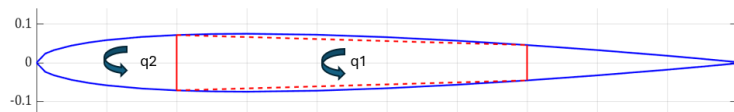


Figure 59: Iteration 3 results



Figure 60: Iteration 4 results

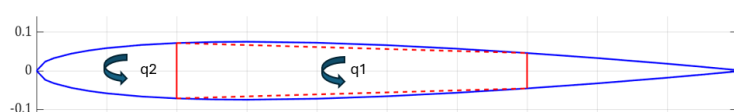


Figure 61: Iteration 5 results

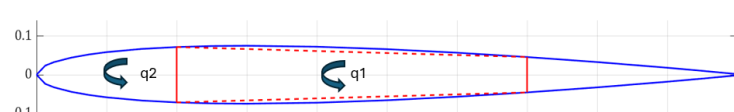


Figure 62: Final Iteration results

A Appendix D - Code

Click Link Below:
Github Repository Containing All Code Used